RESEARCH ARTICLE SUMMARY

PLANT SCIENCE

Structure of the activated ROQ1 resistosome directly recognizing the pathogen effector XopQ

Raoul Martin*, Tiancong Qi*, Haibo Zhang, Furong Liu, Miles King, Claire Toth, Eva Nogales†, Brian J. Staskawicz†

INTRODUCTION: Plants and animals respond to pathogen invasion through intracellular nucleotide-binding leucine-rich repeat receptors (NLRs) that directly interact with pathogen proteins or indirectly detect pathogen-derived alterations in the host proteome. Upon recognition of pathogen invasion, NLRs trigger an immune response that resolves in a variety of ways depending on the type of NLR being activated. The overall architecture of NLRs is highly conserved, consisting of a C-terminal leucine-rich repeat (LRR) platform that determines substrate specificity and a central nucleotide-binding oligomerization domain. The N-terminal domain varies between NLRs and determines the mechanism used by the host to activate the immune response. Thus, NLRs in plants have been classified according to their N-terminal domain into Toll/interleukin 1 receptor (TIR) NLRs (TNLs), coiled-coil NLRs (CNLs), and RPW8-like coiled-coil NLRs (RNLs). Pathogen detection and oligomerization of the NLR activates these N-terminal domains by bringing them in close contact. In all three cases, association of the N-terminal domain leads to localized cell death and expression of disease resistance. The TIR domains of TNLs have been shown to have oligomerization-dependent NADase activity that is required for promoting cell death, but it is not understood how the interactions between TIR domains renders them catalytically active.

RATIONALE: The structure of the ROQ1 (recognition of XopQ 1)–XopQ (*Xanthomonas* outer protein Q) complex, an immune receptor bound to its pathogen substrate, was used as a model to study the mechanism of direct binding, oligomerization, and TIR domain activation of TNLs. ROQ1 has been shown to physically interact with the *Xanthomonas* effector XopQ, causing it to oligomerize and trigger a TIR-dependent hypersensitive cell death response. We coexpressed, extracted, and purified the assembled ROQ1-XopQ complex from ROQ1's native host, *Nicotiana benthamiana*, and solved its structure by cryo–electron microscopy to 3.8-Å resolution. The interactions described in our structure were further confirmed by in vivo mutational analysis.

RESULTS: Our structure reveals that ROQ1 forms a tetrameric resistosome upon recognizing XopQ. The LRR and a post-LRR domain named the C-terminal jelly-roll/Ig-like domain (C-JID), form a horseshoe-shaped scaffold that curls around the pathogen effector, thereby recognizing multiple regions of the substrate. Binding of the ROQ1 LRR to XopQ occurs through surface-exposed residues that make up the scaffold of the domain, as well as an elongated loop between two LRRs that forms a small amphipathic α-helix at the site of interaction. The mode of substrate recognition by the C-JID is reminiscent of that used by immunoglobulins to bind their antigen. Similar to the complementary-determining regions of antibodies, interconnecting loops emerging from the C-JID β-sandwich structure make substrate-specific contacts with XopQ. In particular, an extended loop of the C-JID dives into the active-site cleft of XopQ and interacts with conserved residues required for nucleoside binding, suggesting that ROQ1 not only recognizes its substrate but also inhibits its ligand-binding function.

The nucleotide-binding domain (NBD), helical domain 1 (HD1) and the winged-helix domain (WHD), termed NB-ARC because of their presence in Apaf-1, R proteins, and CED-4 (ARC), are responsible for ROQ1 oligomerization in an ATP-bound state. Individual protomers intercalate in a similar fashion as found in other NLR structures, promoting association between the N-terminal TIR domains. The TIR domains bind to each other through two distinct interfaces (called AE and BE), causing them to form a dimer of dimers. BE-interface contacts cause a conformational rearrangement in a loop, called the BB-loop, at the periphery of the TIR domain active site that exposes the putative catalytic glutamate that is suggested to cleave NAD$^+$. These results provide a rationale for the previously determined oligomerization dependence of TIR domain NADase activity.

CONCLUSION: We propose a step-by-step mechanism for ROQ1 immune signaling based on our structure of the activated complex and on previous biochemical studies. The LRR and C-JID of ROQ1 recognize the pathogen effector through direct contacts with its surface and active-site residues. Detection of the substrate releases autoinhibitory contacts between the NB-ARC domain and the LRR, allowing the NB-ARC domain to transition to an ATP-bound, oligomerization-prone state. Complex assembly brings the TIR domains in close contact, leading to opening of the NADase active site in an interface-dependent manner. Cleavage of NAD$^+$ by the TIR domain results in the release of adenosine diphosphate ribose, a signaling molecule that triggers cytosolic Ca^{2+} influx, a widely used chemical cue in response to various biotic and abiotic stresses, leading to downstream activation of localized cell death and disease resistance. ■

The list of author affiliations is available in the full article online.
*These authors contributed equally to this work.
†Corresponding author. Email: enogales@lbl.gov (E.N.); stask@berkeley.edu (B.J.S.)

Cite this article as: R. Martin *et al*., *Science* **370**, eabd9993 (2020). DOI: 10.1126/science.abd9993

READ THE FULL ARTICLE AT
https://doi.org/10.1126/science.abd9993

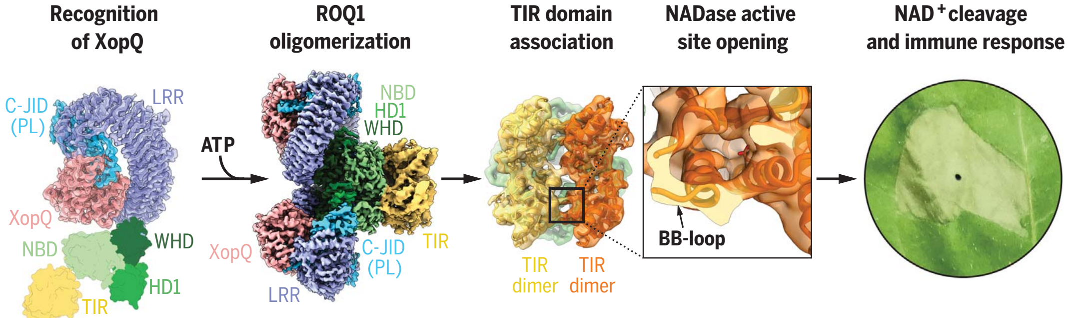

Proposed mechanism of ROQ1 activation. The LRR and C-JID of ROQ1 recognize the pathogen effector XopQ. ROQ1 oligomerizes through the NB-ARC domain (NBD, HD1, WHD) in an ATP-bound state. TIR domain association causes a conformational rearrangement of the BB-loop and opens the NADase active site. Catalytic activity of the TIR domains further signals the immune response, resulting in cell death.

RESEARCH ARTICLE

PLANT SCIENCE

Structure of the activated ROQ1 resistosome directly recognizing the pathogen effector XopQ

Raoul Martin[1,2]*, Tiancong Qi[3,4]*, Haibo Zhang[3], Furong Liu[5], Miles King[5], Claire Toth[6], Eva Nogales[2,6,7,8]†, Brian J. Staskawicz[4,5]†

Plants and animals detect pathogen infection using intracellular nucleotide-binding leucine-rich repeat receptors (NLRs) that directly or indirectly recognize pathogen effectors and activate an immune response. How effector sensing triggers NLR activation remains poorly understood. Here we describe the 3.8-angstrom-resolution cryo–electron microscopy structure of the activated ROQ1 (recognition of XopQ 1), an NLR native to *Nicotiana benthamiana* with a Toll-like interleukin-1 receptor (TIR) domain bound to the *Xanthomonas euvesicatoria* effector XopQ (*Xanthomonas* outer protein Q). ROQ1 directly binds to both the predicted active site and surface residues of XopQ while forming a tetrameric resistosome that brings together the TIR domains for downstream immune signaling. Our results suggest a mechanism for the direct recognition of effectors by NLRs leading to the oligomerization-dependent activation of a plant resistosome and signaling by the TIR domain.

Plants have a sophisticated and finely tuned innate immune system that recognizes invading phytopathogens to protect from infection and disease. Pathogen recognition is facilitated by both membrane-anchored pattern recognition receptors and intracellular innate immune receptors ([1](#)). The latter include the nucleotide-binding leucine-rich repeat receptors (NLRs) ([2](#)). Although some NLR immune receptors directly bind pathogen effector proteins, others, such as ZAR1, monitor effector-mediated alterations of host targets to activate effector-triggered immunity (ETI) ([3](#)–[5](#)). ETI activation is often accompanied by localized cell death referred to as the hypersensitive response (HR). Animals also use NLR proteins as intracellular immune receptors to recognize potential pathogens, and the NLR domain architecture is highly conserved, with each region playing a specific role in its mechanism of action ([6](#)). Plant NLRs generally consist of three domains: an N-terminal region that is either a coiled-coil (CC) domain or a Toll-like interleukin-1 receptor (TIR) domain, a central nucleotide-binding (NB) domain conserved in APAF-1, other R-proteins, and CED-4 (NB-ARC), and the C-terminal leucine-rich repeat (LRR) domain ([2](#)). Plant NLRs are divided into TIR-NLRs (TNLs), CC-NLRs (CNLs), and RPW8-like CC (CC_R)-NLRs (RNLs) based on their N-terminal domains, with experimental evidence consistently suggesting that oligomerization of the N-terminal domains is required for signal transduction and expression of disease resistance ([3](#)).

Although the activation mechanism of a plant CNL resistosome has been elucidated ([7](#), [8](#)), the mechanism of TNL activation remains elusive. There is still no structural evidence for TNL resistosome formation. TIR domains of both plant and animal NLRs were reported to have a nicotinamide adenine dinucleotide (NAD^+) nucleosidase activity that requires TIR domain oligomerization to trigger hypersensitive cell death ([9](#), [10](#)). Whether the NADase activity of the TIR domain is fully responsible for ETI activation and why NAD^+ cleaving only happens in the presence of TIR self-association require further investigation.

To further our understanding of the molecular events that control the direct recognition of pathogen effectors and activation of TNL immune receptors, we transiently coexpressed *Xanthomonas euvesicatoria* type III effector XopQ (*Xanthomonas* outer protein Q) and its TNL receptor ROQ1 (recognition of XopQ 1) in *Nicotiana benthamiana eds1-1* mutant leaves, copurified them by sequential affinity chromatography, and solved a 3.8-Å cryo–electron microscopy (cryo-EM) structure of the assembled protein complex. XopQ is highly conserved across various *Xanthomonas* species and has been shown to have nucleoside hydrolase activity, to physically interact with 14-3-3 proteins of the plant host, and to suppress ETI ([11](#)). Nevertheless, the precise mechanism of XopQ that promotes pathogen virulence remains unclear. Recognition of XopQ by ROQ1 has been shown to trigger downstream ETI signal transduction, leading to a hypersensitive cell death response and resistance to pathogen invasion ([11](#), [12](#)). Our structural data reveal that ROQ1 directly binds XopQ to activate a tetrameric resistosome. We identified a series of necessary contacts for XopQ recognition by ROQ1 and describe the structure of a post-LRR (PL) domain that is essential in effector binding. We also describe the overall oligomeric state of ROQ1 and the interfaces formed by the NB-ARC domain in an open conformation. Finally, we provide an explanation for the requirements of oligomerization in TIR activation, which involves opening of the NADase active site in an interface-dependent manner. Together, our results provide the structural basis for direct effector recognition, oligomerization, and activation of TNLs that reveals how these immune receptors detect pathogens and signal an immune response.

Overall structure of the ROQ1 resistosome

XopQ recognition by ROQ1 triggers a rapid cell death response in wild-type *N. benthamiana* leaves, making it difficult to obtain sufficient protein for expression and purification ([11](#)). All plant TNLs require the downstream EDS1 protein to achieve cell death and express disease resistance ([13](#)). To obtain live tissue for protein purification, we transiently coexpressed ROQ1 and XopQ by *Agrobacterium*-mediated transformation in CRISPR-induced *eds1-1* mutants of *N. benthamiana* known to prevent ROQ1-induced cell death ([12](#)). Cryo-EM imaging and analysis of the affinity-purified complex yielded a reconstruction at 3.8-Å overall resolution with C4 symmetry imposed (figs. S1 and S2) and showed that the ROQ1 protomers assemble into a tetrameric, four-leaf clover structure with XopQ present in a 1:1 ratio (Fig. 1). Further image processing was required to allow building of atomic models (fig. S3). We found that the nucleotide-binding domain (NBD), helical domain 1 (HD1), and winged helix domain (WHD) provide the necessary contacts for ROQ1 oligomerization and bring together the four TIR domains. The LRR features the characteristic horseshoe shape and wraps around the XopQ effector protein, recognizing its surface residues. The cryo-EM map also reveals a PL domain at the C-terminal end of the LRR connected by a short 10-residue linker (Figs. 1A and 2). To improve the density of ROQ1 bound to XopQ, we applied symmetry expansion and focused refinement around the LRR-PL-XopQ region (figs. S1 and S3). The improved reconstruction showed that the XopQ effector is in its open conformation, exposing the cleft of the predicted nucleoside hydrolase

---

[1]Biophysics Graduate Group, University of California, Berkeley, CA 94720, USA. [2]QB3, University of California, Berkeley, CA 94720, USA. [3]Center for Plant Biology, School of Life Sciences, Tsinghua University, Beijing 100084, China. [4]Department of Plant and Microbial Biology, University of California, Berkeley, CA 94720 USA. [5]Innovative Genomics Institute, University of California, Berkeley, CA 94720 USA. [6]Department of Molecular and Cellular Biology, University of California, Berkeley, CA 94720, USA. [7]Howard Hughes Medical Institute, University of California, Berkeley, CA 94720, USA. [8]Molecular Biophysics and Integrated Bioimaging Division, Lawrence Berkeley National Laboratory, University of California, Berkeley, CA 94720, USA.
*These authors contributed equally to this work.
†Corresponding author. Email: enogales@lbl.gov (E.N.); stask@berkeley.edu (B.J.S.)

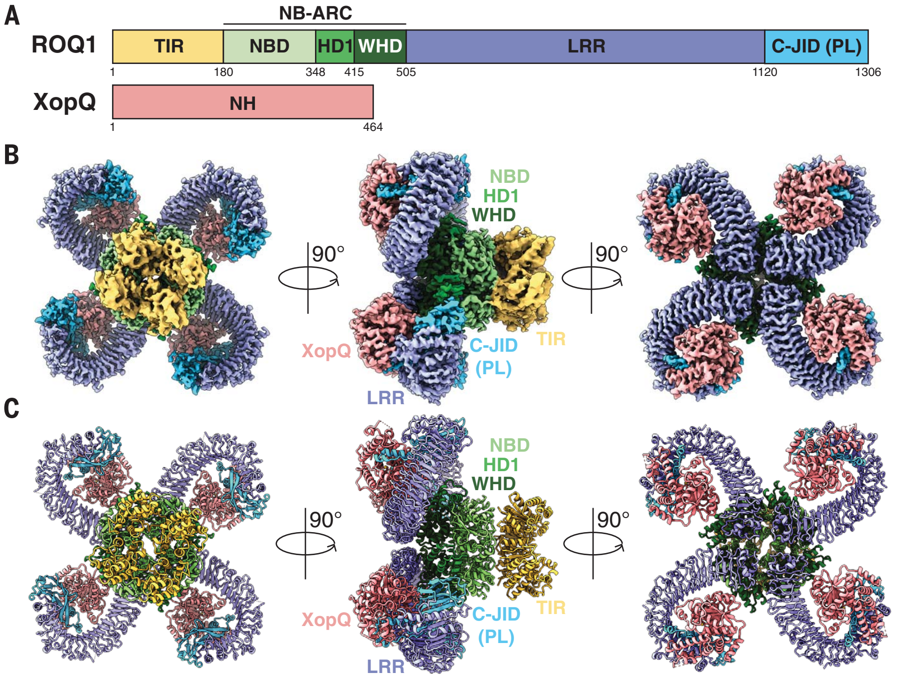

Fig. 1. Overall structure of the ROQ1-XopQ complex. (**A**) Schematic representations of ROQ1 and XopQ with color-coded domain architecture: TIR, yellow; NB-ARC NDB, HD1, and WHD, light green, green, and dark green, respectively; LRR, violet; C-JID (or PL domain), light blue; and XopQ, salmon. (**B** and **C**) Composite density map of the ROQ1-XopQ complex from three cryo-EM reconstructions (B) and corresponding atomic model (C) shown in three orthogonal views. Colors are according to the nomenclature in (A).

active site (Fig. 2E). XopQ's specific substrate remains unidentified, but previous studies have shown that XopQ binds adenosine diphosphate ribose (ADPR), an important immune signaling molecule in plants, consistent with its immunosuppressive function (*14*).

Recognition of XopQ by ROQ1

The 24 LRRs of ROQ1 form a 150-Å-long scaffold that bends around XopQ, displaying key contact residues along its surface (Fig. 2). We found that the LRR of ROQ1 interacts with the effector in two different ways. First, in the region where XopQ is in close contact with the LRR scaffold, several side chains exposed on the surface of the LRR directly interact with the substrate (Fig. 2A). A similar mechanism is used by the LRRs of the CNL ZAR1 to recognize RKS1 and TLR3 to recognize double-stranded RNA (*8*, *15*). Most of these residues have large aromatic side chains that recognize hydrophobic patches and grooves on the surface of XopQ. Second, in regions where the LRR scaffold is too far away to interact with the effector directly, we found an elongated linker between two LRRs (LRRs 23 and 24) that reaches over to bind XopQ (Fig. 2C). A small amphipathic α-helix is formed at the site of contact, with hydrophobic side chains recognizing conserved residues at the outer edge of XopQ's active site cleft ($Y311^{XopQ}$, $H433^{XopQ}$) (Fig. 2C). The extended linker then loops back toward the scaffold and forms the next repeat in the LRR. Mutating the residues that form the hydrophobic face of the α-helix ($L1075^{ROQ1}$, $W1079^{ROQ1}$, $I1078^{ROQ1}$) to alanines resulted in loss of the HR phenotype, suggesting that these interactions are critical for XopQ recognition (fig. S4).

A 10-residue linker (amino acids 1120 to 1129) connects the C-terminal end of the LRR to the PL domain, which also interacts with XopQ (Fig. 2, B and D). This domain folds into a β-sandwich, with nine antiparallel β-strands arranged into two β-sheets (fig. S5). The last LRR forms hydrogen bonds with one of the β-strands, thereby rigidifying the conformation between the two domains. Because PLs serving in pathogen detection have been found in other TNLs but remain poorly characterized, we sought to further investigate the possible structural homology of the ROQ1 PL domain with published structures (*16*). Analysis using the CATH database (*17*) revealed proteins with immunoglobulin-like and jelly-roll folds as the closest structural homologs (fig. S5A). Furthermore, the PL domain of RPP1, another TNL, shares a similar structure to the PL domain in ROQ1 (*18*) despite having low sequence identity (14.29%) (fig. S5). The core of this domain in RPP1 also folds into a β-sandwich structure that forms hydrogen bonds with the last β-strand of the LRR (*18*). Both share the same β-strand topology, with the exception of a ninth C-terminal β-strand present in Roq1 (fig. S5B). The major structural differences in the ROQ1 and RPP1 PL domain are found in the loops that interconnect the β-strands and serve to recognize their respective substrates. Domains fused to the C terminus of LRRs are found in many other NLRs (*3*, *16*) and are likely to differ in structure and function. Therefore, to address the specific type of PL domain used by ROQ1 and RPP1, we refer to it as the C-terminal jelly-roll/Ig-like domain (C-JID).

The mode of recognition used by the C-JID to detect the foreign protein is reminiscent of the way immunoglobulins bind to their antigen (fig. S6). Loops emerging from the β-sandwich structure target sites in XopQ to form substrate-specific contacts with the pathogen protein in a manner that resembles the complementarity-determining regions found in antibodies. The loop between β-strands 7 and 8 of the ROQ1 C-JID simultaneously recognizes a hydrophobic pocket through the insertion of an isoleucine ($I1277^{ROQ1}$) and an area of negative potential targeted by $R1280^{ROQ1}$ (Fig. 2B). Disrupting these interactions with a ROQ1 double mutant (R1280D and I1277A) prevented HR in tobacco leaves, suggesting that these interactions are essential for XopQ detection by ROQ1 (fig. S4).

The greatest number of contacts between the C-JID and XopQ are made by a 33-residue loop (amino acids 1163 to 1196) that dives into the active-site cleft of the effector and positions side chains in close contact with conserved sites required for ADPR binding (Fig. 2, D and E) (*14*). We refer to this loop as the NR loop for its ability to bind residues in XopQ responsible for nucleoside recognition. Two α-helical segments of the loop bring together large hydrophobic side chains that interface with the interior lid region of XopQ (Fig. 2, D and E). The conserved XopQ residues targeted in this region ($W361^{XopQ}$, $F366^{XopQ}$, $L345^{XopQ}$) serve to recognize the base moiety of ADPR (*14*). Active-site residues that would otherwise stabilize the α-phosphate of the ligand ($Y311^{XopQ}$ and $Y398^{XopQ}$) are recognized by ROQ1 $V1171^{ROQ1}$, $H1178^{ROQ1}$, and $H1179^{ROQ1}$ (*14*). Additionally, $H1179^{ROQ1}$ interacts with $D120^{XopQ}$, which is involved in the recognition of one of the sugar moieties in ADPR (*14*). In summary, the conserved residues in XopQ involved in recognizing the base, α-phosphate, and ribose moieties in ADPR are targeted by the ROQ1's NR loop. Mutating the NR loop to a short flexible linker (-SGGGSGGS-) resulted in the loss of HR, suggesting that the ROQ1 mutant could no longer recognize XopQ (fig. S4). Comparison of our structure of XopQ, which is in an open state, with the closed, ADPR-bound state (PDB: 4P5F) shows that the NR loop overlaps with ADPR and thus would prevent the ligand from entering the active-site cleft or interacting with XopQ (Fig. 2E). The presence of the NR loop

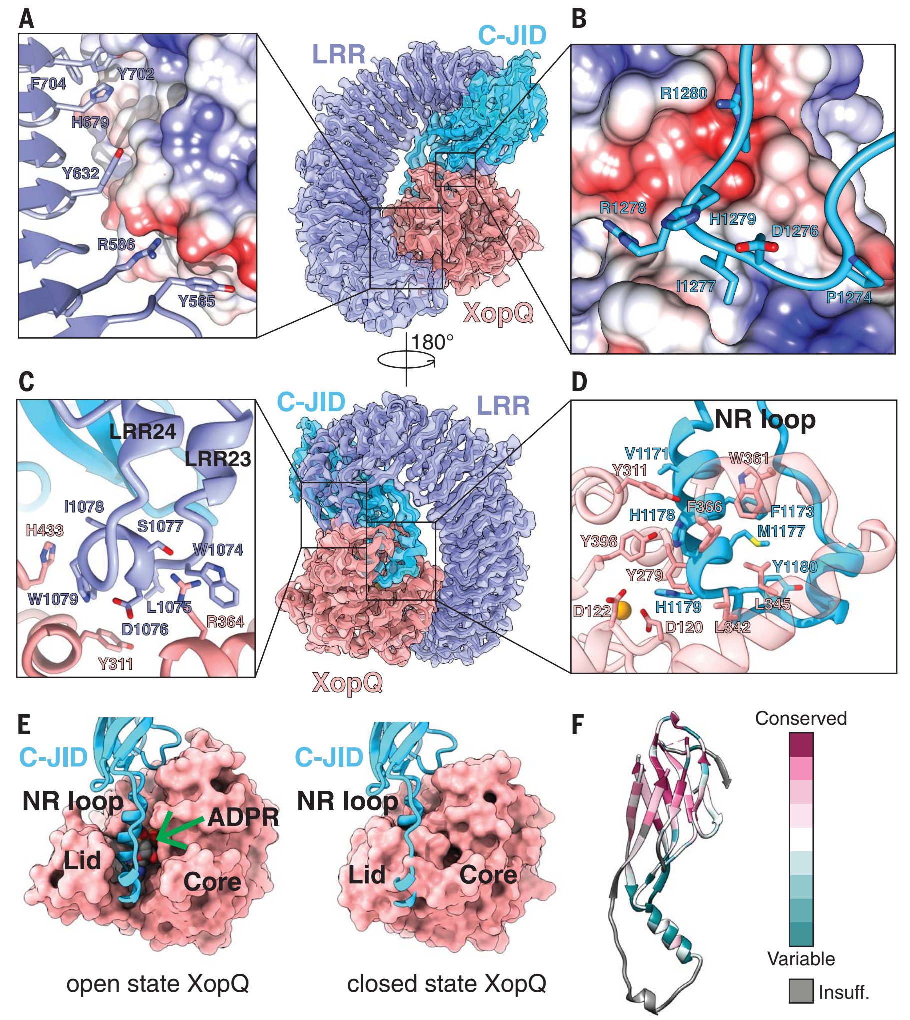

Fig. 2. Structure of the ROQ1 LRR and C-JID (PL domain) binding to XopQ. (**A**) Surface contacts between the N-terminal region of the LRR, shown with a violet ribbon, and XopQ, represented by its Coulombic surface potential. (**B**) Surface contacts made by the loop between β-strands 7 and 8 of the C-JID domain (light blue) and XopQ. (**C**) The elongated LRR between repeats 23 and 24 (violet) interacting with XopQ (salmon). (**D**) Interactions between the NR loop (light blue) and active-site residues of XopQ required for ADPR binding. Catalytic Ca^{2+} is shown in gold. (**E**) Left: Structure of XopQ in the open conformation built from our cryo-EM density, with the NR loop inserted into the active-site cleft. The position of ADPR (green arrow) from the close state of XopQ (PDB: 4P5F) is modeled to show its overlapping position with the NR loop. Right: ADPR-bound, closed state of XopQ. The NR loop is modeled to demonstrate the clashes that would occur upon XopQ closure. (**F**) Residue conservation of the C-JID. Regions where too few sequences aligned to calculate a reliable conservation score are colored in gray (labeled "Insuff.").

may also block XopQ from transitioning to the closed state because the NR loop would clash with the lid region capping the active site. These observations led us to hypothesize that ROQ1 not only recognizes the pathogen effector but may also inhibit its mechanism of ligand binding (*19*).

The C-JID of ROQ1 has a conserved β-sandwich core that may be found in the NLRs of other members of the nightshade family (Fig. 2F). We ran a BLAST search using the sequence of the C-JID (amino acids 1129 to 1306) and found multiple hits corresponding to resistance genes in other species of tobacco, as well as in various species of potatoes, peppers, and morning glories. The more conserved residues are within the strands of the β-sandwich, whereas the loop residues pointing toward XopQ are more variable (Fig. 2F). The NR loop is only found in three other tobacco species, with minor sequence differences (V1171→I, Y1195→F). This pattern of conservation suggests that the variable loops emerging from the C-JID core of related NLRs could serve to recognize different pathogen effectors using a mechanism similar to that used by ROQ1. Such a strategy would be akin to that of sequence variations in the complementarity-determining regions of antibodies that enable them to recognize a diversity of epitopes.

Previous studies suggested that it was difficult to identify mutations in XopQ that could evade ROQ1 recognition (*20*). This is consistent with our results demonstrating that the LRR and C-JID of ROQ1 make multiple contacts with XopQ, suggesting that this gene may be durable in the field and difficult for the pathogen to evade. In the future, these contacts could be modified to build synthetic receptors targeting various pathogen effectors, resulting in new recognitional specificities.

Oligomerization of ROQ1

NLRs are generally thought to exist in an inhibited state mediated by either intra- or intermolecular contacts that prevent oligomerization between protomers and activation of the immune response (*6*, *21*). Structural studies of inactive NLRs suggested that these inhibitory contacts hold the nucleotide-binding region (NBD, HD1, WHD) in a closed state (*7*, *22*, *23*). Upon activation, these interactions must be disrupted to transition to the oligomerization-prone state, where the WHD is moved away from the nucleotide-binding site, thereby displacing the ADP-specific MHD motif on the WHD and allowing adenosine triphosphate (ATP) or deoxyadenosine triphosphate (dATP) binding (NLRs have been shown to bind both ATP and dATP in their active state; in this study, we used ATP) (*8*, *24*–*27*). We expect ROQ1 to be similarly regulated by autoinhibitory contacts with the LRR based on evidence demonstrating that a truncated version of ROQ1 missing the LRR and C-JID regions spontaneously triggers an immune response in the absence of effectors (*12*). We sought to determine whether the C-JID could play a role in autoinhibition. Removing the C-JID of ROQ1 (ΔPL) resulted in loss of HR in planta, suggesting that the LRR, not the C-JID, is involved in making the intramolecular contacts that obstruct a conformational switch to the active state (fig. S4).

Four ROQ1 protomers oligomerize through the NB-ARC domains upon substrate recognition (*12*). Our density map reveals the molecular contacts between the three subdomains of the NB-ARC (NBD, HD1, and WHD) in the context of the resistosome, as well as the presence of ATP at the nucleotide-binding pocket, consistent with an activated state of ROQ1 (Fig. 3). The ATP molecule is stabilized at the interface between the NBD and HD1, with the NBD recognizing the β-phosphate through the canonical P loop (K224 and T225). The two aspartates (D300 and D301) in the Walker B motif are in close proximity to a Mg^{2+} ion that is further coordinated by the β- and γ-phosphate of ATP as well as T225 of the P-loop (Fig. 3A) (*28*). Further recognition of the ligand is provided by R329 of the TTR motif (amino

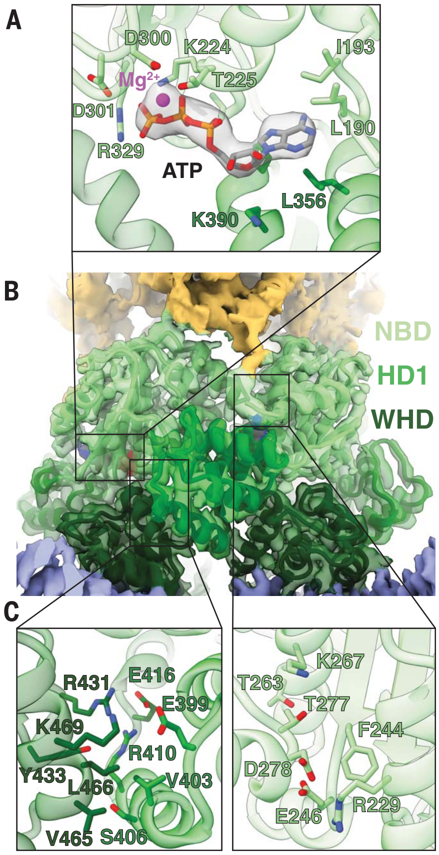

Fig. 3. Oligomerization interfaces between NB-ARC domains. (**A**) ATP modeled in the cryo-EM density (4.8σ) near an oligomerization interface, showing the side chains of residues involved in ATP and Mg^{2+} (magenta) binding. (**B**) Interface between two NB-ARC domains of neighboring protomers. (**C**) Left: Contacts between the WHD and HD1. Right: Contacts between neighboring NBDs. Colors are according to the nomenclature in Fig. 1.

acids 327 to 329) that interacts with the ATP γ-phosphate and by residues forming a pocket around the base moiety (L190, I193, L356). The role of R329 in sensing the ATP molecule is highlighted by a loss of HR phenotype when it is mutated to an alanine (fig. S4).

In agreement with published NLR structures in the active state (*8*, *24*–*27*), the WHD of activated ROQ1 is rotated away from the nucleotide-binding site, thereby displacing the MHD motif and exposing the oligomerization interface (Fig. 3, B and C). This arrangement allows the NBD-HD1 surface of a protomer to intercalate with the NBD-WHD surface of its neighbor. The major interactions involve an HD1-WHD interface and an NBD-NBD interface (Fig. 3C). HD1 binds to the neighboring WHD using a mixture of polar and hydrophobic contacts. Residues in the fourth α-helix of HD1 (amino acids 401 to 413) play an important role in forming the ROQ1 tetramer (Fig. 3C, left). Single point mutations changing the character of these residues (E399R, V403D, and R410A) resulted in loss of HR, suggesting that ROQ1 oligomerization was disrupted (fig. S4). Similar results were observed when mutating a charged residue that brings together NBD domains (R229D) (fig. S4). In other structures of multimeric NLRs (*8*, *24*–*27*), the contacts between the NBDs also involve their N-terminal linker. The equivalent linker in ROQ1 is poorly resolved in our cryo-EM map compared with the surrounding NBD, for which we observed well-defined side-chain densities, indicating that the linker region in ROQ1 is flexible in the tetrameric state. Furthermore, the same linker in other NLRs provides contacts that are in part responsible for properly positioning the NBDs relative to each other. In fact, in NLRs that form larger-order oligomers, the linker forms an α-helix, whereas in smaller complexes such as the pentameric ZAR1, the N-terminal linker forms a slim structured loop without any secondary structure, allowing for the NBD to pack more tightly (fig. S7). Similarly, the poorly defined structure in the ROQ1 linker could explain the tight packing between NBDs that results in tetramerization instead of higher oligomeric states.

Mechanisms have been proposed for the oligomerization of NLRs with differing reliance on nucleotide binding (*21*). In the case of ZAR1, indirect substrate recognition mediated by the guard protein RKS1 causes a conformational change in the NBD and triggers ADP release, but the individual ZAR1 protomers are still unable to oligomerize independently of ATP (*7*, *8*). By contrast, the direct recognition of flagellin by the NLR NAIP5 induces a large conformational transition to the active state (*26*, *29*) and has been shown to activate even when the ATP-binding P-loop motif was mutated (*30*). The structure of the ROQ1 NB-ARC domain closely resembles that of ZAR1 (fig. S8) and shares a 22.2% sequence similarity. Previous studies have also shown that mutation in the P-loop of ROQ1 prevented oligomerization (*12*), suggesting that ATP binding is required for assembly. On the basis of these observations, we expect ROQ1 to follow a similar oligomerization mechanism to ZAR1, in which substrate recognition by the LRR and C-JID of ROQ1 induces a conformational change in the NBD that releases ADP. ATP binding would then be required to transition to the oligomerization-prone state.

TIR domain oligomerization and activation

Tetramerization of the NB-ARC domains brings the TIR domains into close proximity (Fig. 4). The individual TIR domains interact with each other upon resistosome assembly, allowing them to become active NADases and trigger HR (*31*). The mechanism for how this association renders TIRs catalytically active remains poorly understood. Many structural studies on TNL have relied on truncated TIR-containing proteins that are missing the subunits driving oligomerization (*10*, *32*–*36*). Here, we describe a mechanism for TIR association and activation in context of the fully assembled ROQ1 TNL.

Our initial fourfold symmetric reconstruction of ROQ1-XopQ could not clearly resolve the density corresponding to the TIR domains. Further analysis (see the materials and methods) revealed that the four TIR domains do not assemble in a fourfold symmetric fashion, but rather form a twofold symmetric dimer of dimers. The change in symmetry at the TIR domains highlights the importance for flexibility in the linker that connects them to the NBDs, as discussed previously. After adjusting the symmetry for this region and performing focused refinement, the TIR domains reached an overall resolution of 4.6 Å, allowing us to visualize secondary structure elements and trace the polypeptide backbone (figs. S1 and S3). The TIR domains are arranged forming two types of interfaces. First, TIR domains engage in a head-to-head, symmetric interaction involving alpha helices the αA and αE_2 of each protomer [nomenclature of TIR structural motifs as in (*37*), shown as interaction between the same color protomers; Fig, 4, A and B]. This interface, previously called the AE interface, is also found in many crystal structures of isolated plant TIR domains, including RPP1, RUN1, and SNC1 (fig. S9) (*10*, *32*). Consistent with published studies on these plant TNLs, mutating residues in the αA helix of ROQ1 (H30A) disrupts HR and highlights the functional importance of these contacts (fig. S4).

In our structure of ROQ1-XopQ, TIR domains engaged in an AE-AE interaction then further dimerize head-to-tail, forming what is described as the BE interface (*38*) (shown as interactions between the different colored protomers; Fig. 4, A and C). In the BE interaction, the so-called BB-loop (residues between βB and αB) of one TIR domain plugs beneath the loop between αD_3 and αE_1 of the adjacent one (Fig. 4C). Previous mutational analyses already demonstrated a functionally important role for the BB-loop in TIR domains (*10*, *39*). We further mutated residues in the αD_3-αE_1 loop (I151A and G153A) that are in close contact with the BB-loop and found that they independently resulted in loss of the HR phenotype (fig. S4).

Association between plant TIR domains at the DE surface (formed in part by the αD_3-αE_1 loop) has previously been observed in crystallographic studies, but their conformations are different from the ones defined by our cryo-EM analysis. For example, the TIR domains of RPP1, SNC1, and L6 face each other head-to-head at their DE surfaces with different rotational angles relative to each other

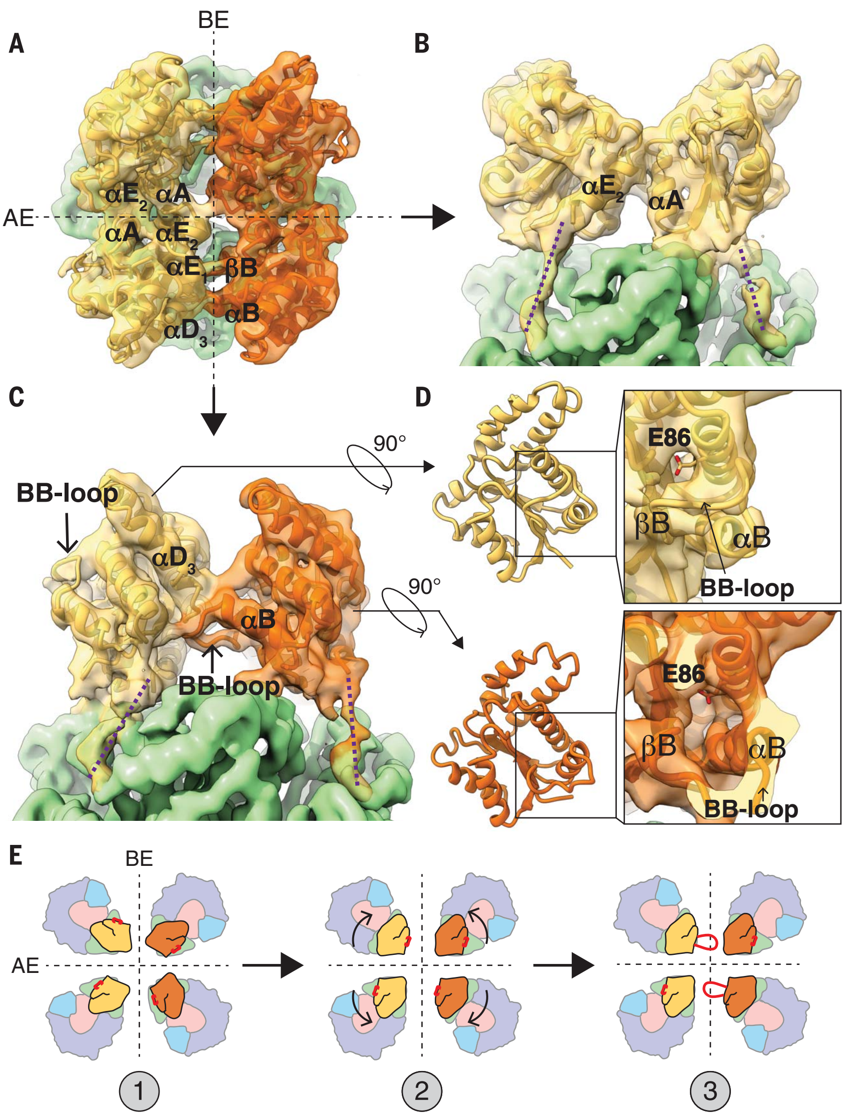

Fig. 4. TIR domain interfaces and conformational rearrangement of the BB-loop. (**A**) Top view of ROQ1 displaying the four TIR domains organized as a dimer of dimers (each symmetric dimer shown in distinct yellow and orange). The two interfaces are marked with black dotted lines; the AE interface is formed between TIR domains shown in the same color. (**B**) Orthogonal view from (A) of the AE interface. (**C**) Orthogonal view from (A) of the BE interface marking the BB-loop positioned under the αD_3 to αE_1 helices. The proposed paths of the protein chain linking the TIR domain to the NBD are shown with purple dotted lines. (**D**) Top: NADase active site of a TIR domain for which the BB-loop is not interfacing with the DE surface. Bottom: Conformational rearrangement in the BB-loop bound to the DE surface. The side chain of the putative catalytic glutamate (E86) is shown in stick representation. (**E**) Hypothetical mechanism of TIR oligomerization with the position of the BB-loop in red. (1) Individual TIR domains are brought in close proximity. (2) TIR domains recognize each other at the AE and BE interface. (3) Assembly causes the conformational rearrangement in the BB-loop that opens the NADase active site. A Gaussian filter was applied to the map in (A) to (D) (width 1.5 Å) to reduce noise.

instead of interacting in a head-to-tail fashion (*32*), perhaps because the TIR domains were visualized in isolation and the NB-ARC domain responsible for driving oligomerization was truncated. These studies highlighted the importance of the DE surface in plant TIR domain oligomerization, but the proper interactions remained unclear because of the variability in conformation between structures. The BE interaction is found in more distant phyla. The crystal structures of TIR domains from the human SARM1 (*10*) and MAL (*40*) proteins, as well as TRR-2 (unpublished, PDB: 4W8G and 4W8H) from *Hydra magnipapillata* share a similar BB-loop conformation to that found in the activated ROQ1 tetramer, in which it fits under the αD_3-αE_1 loop (fig. S10). This structural relationship suggests shared mechanistic features for TIR domain assembly and activation between animals and plants. In fact, the human SARM1 TIR domains simultaneously form AE and BE interfaces in the crystal lattice (figs. S9 and S10) (*10*).

Our structure now demonstrates that the BB-loop takes on two different conformations within the activated ROQ1 tetramer and undergoes a conformational switch as TIR domains interact at a BE interface. In the protomer in which the BB-loop is unbound (the one that is contributing to the BE contacts through its DE surface), it is seen in an upward position along the rim of the NADase active site (Fig. 4C). This conformation is the same as that found in the TIR crystal structures lacking BE contacts (*32*). In the other protomer, the BB-loop interfacing with the adjacent DE surface has been repositioned by a downward motion of ~12 Å (Fig. 4D, bottom). A highly conserved glycine residue (G52$^{\text{ROQ1}}$) in the BB-loop likely provides the flexibility required to undergo this conformational switch (fig. S11). Mutating this glycine to a proline resulted in loss of HR (fig. S4). Similarly, mutating the equivalent glycine in SARM1 (G601P) was shown to hinder flexibility and prevent a transition to the engaged state, resulting in a defective BE interface with the loop stuck in the upward position and a severe decrease in NADase activity (fig. S11) (*10*).

Repositioning of the BB-loop induced by the BE interface opens the NADase active site (Fig. 4D). Large, positively charged side chains (of K50$^{\text{ROQ1}}$, R51$^{\text{ROQ1}}$, and K53$^{\text{ROQ1}}$) that would otherwise crowd the entrance of the active site are moved down with the BB-loop. The structure of a SARM1 mutant (G601P), in which the BB-loop is trapped in the unengaged state, reveals a lysine inserted inside the active-site cleft; this indicates that these side chains may act to prevent substrate binding (*10*). Furthermore, NADase activity increased when equivalent BB-loop arginines were mutated to alanines in the plant RUN1 TIR domain (*10*). Together, these studies suggest that these large, positively charged side chains serve to inhibit NADase function and must be displaced for TIR activation.

Freeing the active site exposes conserved residues that have been proposed to recognize NAD$^+$ based on biochemical and structural studies using chemical analogs (*9*, *10*). The nicotinamide moiety of the substrate is supposed to fit in the active-site cleft of the TIR domain, bringing the covalently linked ribose in close proximity to the catalytic glutamate. Mutating the putative catalytic glutamate in ROQ1 (E86$^{\text{ROQ1}}$) to an alanine abrogates HR (fig. S4), suggesting loss of NADase activity. No NAD$^+$ was observed in our structure, which could have been cleaved by the activated TIR domain, yet we still observed a small density positioned above the TIR domain active site at the BE interface (fig. S12). An ATP molecule was modeled at this position in Ma *et al.* (*18*). The corresponding density in our map is weak compared with that of neighboring residues (W82), with only part of an ATP molecule fitting in the density even at low contour levels (fig. S12). Therefore, it was left unmodeled. Further investigation will be required to determine the position of NAD$^+$ within the ROQ1 TIR domain active site. Mechanistic details of NAD$^+$ cleavage and product formation remain unresolved and have been found to vary among TIR domains (*31*). The steps in this enzymatic reaction involve breaking the glycosidic bond that connects nicotinamide to ADPR and, in some cases, a structural rearrangement in ADPR that leads to the formation of cyclic-ADPR or variant-cyclic-ADPR (*9*, *41*). ADPR and cyclic-ADPR have been shown to modulate the Ca^{2+} level in plant cells, which is a widely used chemical signal for responding to various biotic and abiotic stresses (*42*).

In the case of the fully assembled ROQ1 TNL, it is clear that the AE and BE interfaces are essential in TIR signaling. Both interfaces align the TIR domains in a conformation inducive to NADase active-site opening (Fig. 4E). Whether this mechanism of TIR association can be applied to other TNL remains to be determined. Similar to ROQ1, the TIR domains of the activated RPP1 tetramer form a dimer of dimers through AE- and BE-interface contacts, causing a rearrangement in the BB-loop (*18*). Nevertheless, there are likely to be alternative ways for TIR domains to assemble based on the number of protomers required to build the active complex, heterocomplex formation with other NLRs, and interface requirements for activation.

Summary

Our structure of the ROQ1-XopQ complex, together with previous biochemical studies, led us to propose a mechanism for TNL immune signaling: (i) both the LRR and C-JID recognize the pathogen effector, at which point the NR loop inserts itself into the active-site cleft of XopQ and targets conserved residues required for nucleoside-binding; (ii) the NB-ARC domain is released by the LRR and undergoes a conformational switch to the ATP-bound oligomerization state; (iii) ROQ1 protomers associate into a four-leaf-clover structure and the TIR domains are brought in close contact; (iv) the TIR domains bind to each other, forming distinct AE and BE interfaces and causing a conformational rearrangement in the BB-loop of two of the subunits; and (v) the NADase active site is exposed, allowing for the cleavage of NAD$^+$. Future work will be required to identify the exact molecular species produced by the TIR domains and how they are used by the immune system of the host to trigger a response to pathogen invasion.

Methods summary

ROQ1-3Flag and StrepII-XopQ were transformed into *Agrobacterium* GV3101 and coexpressed in *N. benthamiana eds1-1* mutant leaves through transient agroinfiltration. Leave tissue was harvested 30 hours after infiltration and ground with a mortar and pestle. The powdered leaf material was then resuspended in a buffer supplemented with protease inhibitors and further lysed by sonication. Two rounds of centrifugation were required to separate cell debris from the soluble fraction of the lysate. Purification of the assembled Roq1-XopQ complex was performed by sequential affinity chromatography. First, we selected for ROQ1-3Flag by Flag-immunoprecipitation. Strep-tactin resin was then used to capture the StrepII-XopQ containing complex. Individual steps can be visualized on a SDS–polyacrylamide gel electrophoresis gel in fig. S13.

The purified Roq1-XopQ complex was deposited on a freshly plasma cleaned holey carbon grid (QUANTIFOIL R2/2) coated with a thin layer of carbon. The original buffer used in the purification of the sample was removed and replaced with a similar buffer containing 3% trehalose instead of NP-40 and glycerol. The grid was mounted onto a Thermo Fisher Scientific Mk. IV Vitrobot, blotted, and plunged-frozen in liquid ethane.

Data were collected using a Titan Krios cryo–electron microscope operating at 300 kV and equipped with a K3 direct electron detector camera mounted behind a BioQuantum energy filter. A total of 11,134 dose-fractionated movies were acquired in superresolution counting mode, with an electron exposure of 50 e$^-$/Å^2 and defocus values ranging from –0.9 to –2.5 μm.

All processing steps were done in Relion 3.1 (*43*). CTF fits were calculated in Gctf (*44*). Particles were selected from the motion corrected micrographs (*45*) using an unbiased Laplacian-of-Gaussian autopicker and were subjected to an initial round of 3D classification. One more round of refinement followed by alignment-free 3D classification resulted in a class of 15,263 particles with a broad distribution of projection directions that converged to 3.8-Å resolution [Fourier shell correlation (FSC) = 0.143]. Symmetry expansion and focused refinement were required to resolve the LRR-PL-XopQ and TIR domain regions at a resolution of 3.8 and 4.6 Å, respectively. A detailed procedure is described in figs. S2 and S3.

Individual models were built for each of the three cryo-EM reconstructions. An initial model for the NB-ARC domain, TIR domain, and XopQ were generated using structures of homologous proteins in the PDB (6J5T, 5KU7, and 4KL0, respectively). The LRR and PL domain of ROQ1 were built manually in COOT (*46*). Models were refined and validated in Phenix (*47*). A final model versus map FSC was calculated using MTRIAGE (*48*). Model validation statistics can be found in table S1.

For HR phenotype observation, ROQ1-3Flag mutants and StrepII-XopQ were transiently coexpressed in *N. tabacum roq1-1* mutant leaves through *Agrobacterium*-mediated transformation. HR phenotypes were observed and imaged 2 days after infiltration. To test for protein expression, ROQ1-3Flag mutants and StrepII-XopQ were coexpressed and extracted from *N. benthamiana eds1-1* mutant leaves and detected by Western blotting.

Conservation scores for residues in the ROQ1 C-JID were calculated in Consurf (*49*) from a multiple sequence alignment provided in the supplementary materials (sequence alignment file S1).

REFERENCES AND NOTES

1. J. L. Dangl, D. M. Horvath, B. J. Staskawicz, Pivoting the plant immune system from dissection to deployment. *Science* **341**, 746–751 (2013). doi: 10.1126/science.1236011; pmid: 23950531
2. J. Wang, J. Chai, Structural insights into the plant immune receptors PRRs and NLRs. *Plant Physiol.* **182**, 1566–1581 (2020). doi: 10.1104/pp.19.01252; pmid: 32047048
3. J. Tamborski, K. V. Krasileva, Evolution of plant NLRs: From natural history to precise modifications. *Annu. Rev. Plant Biol.* **71**, 355–378 (2020). doi: 10.1146/annurev-arplant-081519-035901; pmid: 32092278
4. J. M. Feehan, B. Castel, A. R. Bentham, J. D. G. Jones, Plant NLRs get by with a little help from their friends. *Curr. Opin. Plant Biol.* **56**, 99–108 (2020). doi: 10.1016/j.pbi.2020.04.006; pmid: 32554226
5. L. M. Jubic, S. Saile, O. J. Furzer, F. El Kasmi, J. L. Dangl, Help wanted: Helper NLRs and plant immune responses. *Curr. Opin. Plant Biol.* **50**, 82–94 (2019). doi: 10.1016/j.pbi.2019.03.013; pmid: 31063902
6. J. D. G. Jones, R. E. Vance, J. L. Dangl, Intracellular innate immune surveillance devices in plants and animals. *Science* **354**, aaf6395 (2016). doi: 10.1126/science.aaf6395; pmid: 27934708
7. J. Wang *et al.*, Ligand-triggered allosteric ADP release primes a plant NLR complex. *Science* **364**, eaav5868 (2019). doi: 10.1126/science.aav5868; pmid: 30948526
8. J. Wang *et al.*, Reconstitution and structure of a plant NLR resistosome conferring immunity. *Science* **364**, eaav5870 (2019). doi: 10.1126/science.aav5870; pmid: 30948527
9. L. Wan *et al.*, TIR domains of plant immune receptors are NAD$^+$-cleaving enzymes that promote cell death. *Science* **365**, 799–803 (2019). doi: 10.1126/science.aax1771; pmid: 31439793
10. S. Horsefield *et al.*, NAD$^+$ cleavage activity by animal and plant TIR domains in cell death pathways. *Science* **365**, 793–799 (2019). doi: 10.1126/science.aax1911; pmid: 31439792
11. A. Schultink, T. Qi, A. Lee, A. D. Steinbrenner, B. Staskawicz, Roq1 mediates recognition of the Xanthomonas and Pseudomonas effector proteins XopQ and HopQ1. *Plant J.* **92**, 787–795 (2017). doi: 10.1111/tpj.13715; pmid: 28891100
12. T. Qi *et al.*, NRG1 functions downstream of EDS1 to regulate TIR-NLR-mediated plant immunity in *Nicotiana benthamiana*. *Proc. Natl. Acad. Sci. U.S.A.* **115**, E10979–E10987 (2018). doi: 10.1073/pnas.1814856115; pmid: 30373842
13. D. Lapin, D. D. Bhandari, J. E. Parker, Origins and immunity networking functions of EDS1 family proteins. *Annu. Rev. Phytopathol.* **58**, 253–276 (2020). doi: 10.1146/annurev-phyto-010820-012840; pmid: 32396762
14. S. Yu, I. Hwang, S. Rhee, The crystal structure of type III effector protein XopQ from Xanthomonas oryzae complexed with adenosine diphosphate ribose. *Proteins* **82**, 2910–2914 (2014). doi: 10.1002/prot.24656; pmid: 25079351
15. L. Liu *et al.*, Structural basis of toll-like receptor 3 signaling with double-stranded RNA. *Science* **320**, 379–381 (2008). doi: 10.1126/science.1155406; pmid: 18420935

16. C. Van Ghelder, D. Esmenjaud, TNL genes in peach: Insights into the post-LRR domain. *BMC Genomics* **17**, 317 (2016). doi: 10.1186/s12864-016-2635-0; pmid: 27129402
17. I. Sillitoe *et al*., CATH: Expanding the horizons of structure-based functional annotations for genome sequences. *Nucleic Acids Res.* **47** (D1), D280–D284 (2019). doi: 10.1093/nar/gky1097; pmid: 30398663
18. S. Ma *et al*., Direct pathogen-induced assembly of an NLR immune receptor complex to form a holoenzyme. *Science* 10.1126/science.abe3069 (2020). doi: 10.1126/science.abe3069
19. W. Li, Y.-H. Chiang, G. Coaker, The HopQ1 effector's nucleoside hydrolase-like domain is required for bacterial virulence in arabidopsis and tomato, but not host recognition in tobacco. *PLOS ONE* **8**, e59684 (2013). doi: 10.1371/journal.pone.0059684; pmid: 23555744
20. N. Adlung, U. Bonas, Dissecting virulence function from recognition: Cell death suppression in Nicotiana benthamiana by XopQ/HopQ1-family effectors relies on EDS1-dependent immunity. *Plant J.* **91**, 430–442 (2017). doi: 10.1111/tpj.13578; pmid: 28423458
21. Y. Xiong, Z. Han, J. Chai, Resistosome and inflammasome: Platforms mediating innate immunity. *Curr. Opin. Plant Biol.* **56**, 47–55 (2020). doi: 10.1016/j.pbi.2020.03.010; pmid: 32554225
22. J. F. C. Steele, R. K. Hughes, M. J. Banfield, Structural and biochemical studies of an NB-ARC domain from a plant NLR immune receptor. *PLOS ONE* **14**, e0221226 (2019). doi: 10.1371/journal.pone.0221226; pmid: 31461469
23. Z. Hu *et al*., Crystal structure of NLRC4 reveals its autoinhibition mechanism. *Science* **341**, 172–175 (2013). doi: 10.1126/science.1236381; pmid: 23765277
24. Y. Pang *et al*., Structure of the apoptosome: Mechanistic insights into activation of an initiator caspase from Drosophila. *Genes Dev.* **29**, 277–287 (2015). doi: 10.1101/gad.255877.114; pmid: 25644603
25. S. Qi *et al*., Crystal structure of the *Caenorhabditis elegans* apoptosome reveals an octameric assembly of CED-4. *Cell* **141**, 446–457 (2010). doi: 10.1016/j.cell.2010.03.017; pmid: 20434985
26. J. L. Tenthorey *et al*., The structural basis of flagellin detection by NAIP5: A strategy to limit pathogen immune evasion. *Science* **358**, 888–893 (2017). doi: 10.1126/science.aao1140; pmid: 29146805
27. L. Zhang *et al*., Cryo-EM structure of the activated NAIP2-NLRC4 inflammasome reveals nucleated polymerization. *Science* **350**, 404–409 (2015). doi: 10.1126/science.aac5789; pmid: 26449474
28. V. Bonardi, K. Cherkis, M. T. Nishimura, J. L. Dangl, A new eye on NLR proteins: Focused on clarity or diffused by complexity? *Curr. Opin. Immunol.* **24**, 41–50 (2012). doi: 10.1016/j.coi.2011.12.006; pmid: 22305607
29. X. Yang *et al*., Structural basis for specific flagellin recognition by the NLR protein NAIP5. *Cell Res.* **28**, 35–47 (2018). doi: 10.1038/cr.2017.148; pmid: 29182158
30. E. F. Halff *et al*., Formation and structure of a NAIP5-NLRC4 inflammasome induced by direct interactions with conserved N- and C-terminal regions of flagellin. *J. Biol. Chem.* **287**, 38460–38472 (2012). doi: 10.1074/jbc.M112.393512; pmid: 23012363
31. A. M. Bayless, M. T. Nishimura, Enzymatic functions for Toll/interleukin-1 receptor domain proteins in the plant immune system. *Front. Genet.* **11**, 539 (2020). doi: 10.3389/fgene.2020.00539; pmid: 32582284
32. X. Zhang *et al*., Multiple functional self-association interfaces in plant TIR domains. *Proc. Natl. Acad. Sci. U.S.A.* **114**, E2046–E2052 (2017). doi: 10.1073/pnas.1621248114; pmid: 28159890
33. S. J. Williams *et al*., Structural basis for assembly and function of a heterodimeric plant immune receptor. *Science* **344**, 299–303 (2014). doi: 10.1126/science.1247357; pmid: 24744375
34. K.-G. Hyun, Y. Lee, J. Yoon, H. Yi, J.-J. Song, Crystal structure of Arabidopsis thaliana SNC1 TIR domain. *Biochem. Biophys. Res. Commun.* **481**, 146–152 (2016). doi: 10.1016/j.bbrc.2016.11.004; pmid: 27818198
35. M. Bernoux *et al*., Structural and functional analysis of a plant resistance protein TIR domain reveals interfaces for self-association, signaling, and autoregulation. *Cell Host Microbe* **9**, 200–211 (2011). doi: 10.1016/j.chom.2011.02.009; pmid: 21402359
36. S. J. Williams *et al*., Structure and function of the TIR domain from the grape NLR protein RPV1. *Front. Plant Sci.* **7**, 1850 (2016). pmid: 28008335
37. Y. Xu *et al*., Structural basis for signal transduction by the Toll/interleukin-1 receptor domains. *Nature* **408**, 111–115 (2000). doi: 10.1038/35040600; pmid: 11081518
38. S. Nimma, T. Ve, S. J. Williams, B. Kobe, Towards the structure of the TIR-domain signalosome. *Curr. Opin. Struct. Biol.* **43**, 122–130 (2017). doi: 10.1016/j.sbi.2016.12.014; pmid: 28092811
39. L. Vyncke *et al*., Reconstructing the TIR side of the myddosome: A paradigm for TIR-TIR interactions. *Structure* **24**, 437–447 (2016). doi: 10.1016/j.str.2015.12.018; pmid: 26876098
40. T. Ve *et al*., Structural basis of TIR-domain-assembly formation in MAL- and MyD88-dependent TLR4 signaling. *Nat. Struct. Mol. Biol.* **24**, 743–751 (2017). doi: 10.1038/nsmb.3444; pmid: 28759049
41. K. Essuman *et al*., TIR domain proteins are an ancient family of NAD$^+$-consuming enzymes. *Curr. Biol.* **28**, 421–430.e4 (2018). doi: 10.1016/j.cub.2017.12.024; pmid: 29395922
42. Y. Wu *et al*., Abscisic acid signaling through cyclic ADP-ribose in plants. *Science* **278**, 2126–2130 (1997). doi: 10.1126/science.278.5346.2126; pmid: 9405349
43. S. H. W. Scheres, RELION: Implementation of a Bayesian approach to cryo-EM structure determination. *J. Struct. Biol.* **180**, 519–530 (2012). doi: 10.1016/j.jsb.2012.09.006; pmid: 23000701
44. K. Zhang, Gctf: Real-time CTF determination and correction. *J. Struct. Biol.* **193**, 1–12 (2016). doi: 10.1016/j.jsb.2015.11.003; pmid: 26592709
45. S. Q. Zheng *et al*., MotionCor2: Anisotropic correction of beam-induced motion for improved cryo-electron microscopy. *Nat. Methods* **14**, 331–332 (2017). doi: 10.1038/nmeth.4193; pmid: 28250466
46. P. Emsley, K. Cowtan, Coot: Model-building tools for molecular graphics. *Acta Crystallogr. D Biol. Crystallogr.* **60**, 2126–2132 (2004). doi: 10.1107/S0907444904019158; pmid: 15572765
47. P. D. Adams *et al*., PHENIX: Building new software for automated crystallographic structure determination. *Acta Crystallogr. D Biol. Crystallogr.* **58**, 1948–1954 (2002). doi: 10.1107/S0907444902016657; pmid: 12393927
48. P. V. Afonine *et al*., New tools for the analysis and validation of cryo-EM maps and atomic models. *Acta Crystallogr. D Struct. Biol.* **74**, 814–840 (2018). doi: 10.1107/S2059798318009324; pmid: 30198894
49. H. Ashkenazy *et al*., ConSurf 2016: An improved methodology to estimate and visualize evolutionary conservation in macromolecules. *Nucleic Acids Res.* **44** (W1), W344–W350 (2016). doi: 10.1093/nar/gkw408; pmid: 27166375

ACKNOWLEDGMENTS

We dedicate this work to the memory of André Martin (1929–2020). We thank P. Grob and D. Toso for electron microscopy support; A. Chintangal and P. Tobias for computational support; N. Haloupek and P. Grob for advice with cryo-EM grid preparation of NLR samples; B. Greber for advice with data processing and with model building and refinement; K. Krasileva, D. Prigozhin, and K. Verster for useful discussion on PL domain conservation and LRR-effector interactions; and B. Kobe for useful discussion on TIR domains. Data were collected at the BACEM facility, Berkeley QB3. Molecular graphics and analyses were performed with UCSF Chimera and UCSF ChimeraX. **Funding:** This work was supported by the Founders Fund from the Innovative Genomics Institute of the University of California–Berkeley (to B.J.S.) and by funds from the Tsinghua-Peking Center for Life Sciences (to T.Q.). T.Q. was supported by a Tang Distinguished Scholarship from the University of California–Berkeley. E.N. is a Howard Hughes Medical Institute Investigator. **Author contributions:** E.N. and B.J.S. supervised the work. T.Q. constructed ROQ1 and XopQ vectors and expressed the ROQ1-XopQ protein complex in *N. benthamiana*. R.M. and T.Q. established purification protocols and purified the ROQ1-XopQ complex. R.M. prepared cryo-EM grids, collected and processed cryo-EM data, and performed model building, refinement, and interpretation. C.T. assisted in purification and grid making. R.M., T.Q., H.Z., and F.L. constructed ROQ1 mutants. T.Q. and H.Z. detected protein expression and HR phenotypes. M.K. assisted in ROQ1 and XopQ protein expression in *N. benthamiana*. R.M. wrote the initial draft of the manuscript. All authors contributed to the final version of the paper. **Competing interests:** B.J.S. is the scientific cofounder and serves on the board of directors of Mendel Biotechnology and is on the scientific advisory boards of Verinomics and the Sainsbury Laboratory. R.M. and B.J.S. are inventors on a patent application held by the University of California that covers the ability to engineer new plant immune receptors. **Data and materials availability:** Materials are available from B.J.S. CryoEM density maps and fitted models have been deposited in the Electron Microscopy Data Bank (EMDB) and the Protein Data Bank (PDB). The maps for initial reconstruction of the ROQ1-XopQ complex, focused refinement around the LRR-C-JID-XopQ region, and TIR domains have been deposited with the EMDB accession codes 22381, 22380, and 22383, respectively. The refined coordinate models have been deposited with PDB accession codes 7JLV, 7JLU, and 7JLX, respectively. All other data are available either in the main paper or the supplementary materials.

SUPPLEMENTARY MATERIALS

science.sciencemag.org/content/370/6521/eabd9993/suppl/DC1
Materials and Methods
Figs. S1 to S13
Table S1
References (*50*–*58*)
Movie S1
Sequence Alignment File S1
MDAR Reproducibility Checklist

View/request a protocol for this paper from *Bio-protocol*.

31 July 2020; accepted 19 October 2020
10.1126/science.abd9993

Science

Structure of the activated ROQ1 resistosome directly recognizing the pathogen effector XopQ

Raoul Martin, Tiancong Qi, Haibo Zhang, Furong Liu, Miles King, Claire Toth, Eva Nogales and Brian J. Staskawicz

Science **370** (6521), eabd9993.
DOI: 10.1126/science.abd9993

Tetrameric immune receptors

Nucleotide-binding/leucine-rich repeat (NLR) immune receptors detect pathogen effectors and trigger a plant's immune response. Two groups have now defined the structures of two NLRs that carry Toll-like interleukin-1 receptor (TIR) domains (TIR-NLRs) (see the Perspective by Tian and Li). Ma *et al.* studied the *Arabidopsis thaliana* TIR-NLR RPP1 (recognition of *Peronospora parasitica* 1) and its response to effectors from an oomycete pathogen. Martin *et al.* studied the *Nicotiana benthamiana* TIR-NLR ROQ1 (recognition of XopQ 1) and its response to the *Xanthomonas* effector. Both groups found that these TIR-NLRs formed tetramers that, when activated by binding to the pathogen effector, exposed the active site of a nicotinamide adenine dinucleoside (NAD) hydrolase. Thus, recognition of the pathogen effector initiates NAD hydrolysis and begins the immune response.

Science, this issue p. eabe3069, p. eabd9993; see also p. 1163

ARTICLE TOOLS	http://science.sciencemag.org/content/370/6521/eabd9993
SUPPLEMENTARY MATERIALS	http://science.sciencemag.org/content/suppl/2020/12/02/370.6521.eabd9993.DC1
RELATED CONTENT	http://science.sciencemag.org/content/sci/370/6521/eabe3069.full http://science.sciencemag.org/content/sci/370/6521/1163.full
REFERENCES	This article cites 58 articles, 17 of which you can access for free http://science.sciencemag.org/content/370/6521/eabd9993#BIBL
PERMISSIONS	http://www.sciencemag.org/help/reprints-and-permissions

---

Science (print ISSN 0036-8075; online ISSN 1095-9203) is published by the American Association for the Advancement of Science, 1200 New York Avenue NW, Washington, DC 20005. The title *Science* is a registered trademark of AAAS.

science.sciencemag.org/content/370/6521/eabd9993/suppl/DC1

Supplementary Materials for

Structure of the activated ROQ1 resistosome directly recognizing the pathogen effector XopQ

Raoul Martin*, Tiancong Qi*, Haibo Zhang, Furong Liu, Miles King, Claire Toth, Eva Nogales†, Brian J. Staskawicz†

*These authors contributed equally to this work.
†Corresponding author. Email: enogales@lbl.gov (E.N.); stask@berkeley.edu (B.J.S.)

Published 4 December 2020, *Science* **370**, eabd9993 (2020)
DOI: 10.1126/science.abd9993

This PDF file includes:

- Materials and Methods
- Supplementary Text
- Figs. S1 to S13
- Table S1
- Caption for Movie S1
- References

Other Supplementary Material for this manuscript includes the following:
(available at science.sciencemag.org/content/370/6521/eabd9993/suppl/DC1)

- Movie S1 (mp4)
- Sequence Alignment File S1 (PDF)
- MDAR Reproducibility Checklist (PDF)

Materials and Methods

Plant Materials and Growth Conditions

The *N. benthamiana eds1-1* mutant was described as previously (14). The binary vector containing ROQ1 guide sequence (GATGATAAGGAGTTAAAGAG) and Cas9 was described previously (15) was transformed into agrobacterium and used for generating *N. tabacum roq1-1* stable mutant plants by CRISPR-Cas9 gene editing system. *N. benthamiana* and *N. tabacum* plants were grown in a growth chamber under a 8-hr-light/16-hr-dark photoperiod at 23-25℃.

Expression and Purification of the ROQ1-XopQ Complex

ROQ1 and XopQ were fused with C-terminal 3xFlag tag and N-terminal StrepII tag, respectively, and transformed into Agrobacterium GV3101. The agrobacterium GV3101 strains containing ROQ1-3xFlag and StrepII-XopQ were co-inoculated into *N. benthamiana eds1-1* mutant leaves. At 30 hours after infiltration, 200g of leaves were harvested and ground using a mortar and pestle and resuspended in 400 mL of Lysis Buffer (50 mM HEPES pH 7.5, 1 mM EDTA. 5 mM MgCl2, 150 mM NaCl, 10 mM KCl, 0.4% NP40, 5% glycerol, 10 mM DTT) supplemented with protease inhibitors (100 uM PMSF, 1 uM Phosphoramidon, 10 uM 1,10-Phenanthrolin, 1uM Pepstatin A, 10 uM Leupeptin, 2 uM E-64, 10 uM Bestatin and 2 ug/mL Aprotinin). Leaves were further lysed by sonication for 2 min at 20 kHz. The cell lysate was initially centrifuged at 18,000xg for 45 min to pellet large debris and the harvested supernatant was further centrifuged at 40,000xg for 45 min to remove any smaller residuals. The clarified extract was then incubated with 800 µL (bed volume) of ANTI-FLAG M2 affinity gel (Sigma-Aldrich) for 3 hours at 4℃. The gel was washed with 10 CV of Wash Buffer (20 mM HEPES pH 7.5, 1mM EDTA, 5 mM MgCl2, 150 mM NaCl, 10 mM KCl, 0.2% NP-40, 10% glycerol) and the sample was eluted twice by incubating in 1 CV of Wash Buffer supplemented with 300 µg/mL of 3xFlag peptide for 30 min. Each wash and elution was separated from the affinity-resin by centrifugation at 300xg for 5 min. Eluates were pooled and incubated with 20 µL (bed volume) of Strep-Tactin Superflow Plus (Qiagen) resin for 1 hour. The resin was then washed with 10 CV of Wash Buffer and the totality of the sample was eluted in 5 sequential steps by adding 1 CV Wash Buffer supplemented with 10 mM Biotin. Each wash and elution was separated from the affinity-resin by centrifugation at 300xg for 5 min. The protein complex was flash frozen in liquid N_2 and stored at -80˚C. Individual steps can be visualized by SDS-PAGE in Fig. S13. We were unable to accurately measure the final protein concentration due to low amounts of sample.

Sample Preparation for Cryo-EM

QUANTIFOIL R2/2 holey carbon grids were coated with a thin film of continuous carbon (approximately 3 nm thick) and plasma cleaned (Tergeo-EM, PIE Scientific LLC, operating at 15 W for 30 sec in indirect mode) before addition of sample. Because of the low concentration of the ROQ1-XopQ complex in our sample, we attempted to float the carbon-coated grid on the sample drop to enable prolonged incubation to allow attachment of more molecules to the carbon. However, due to the high detergent concentration of the sample buffer, loss of surface tension caused the grids to sink to the bottom of the drop. Therefore, we used a Teflon well to hold 20 µL of sample (supplemented with 1 mM ATP) and deposited the grid in the well carbon side up, upon which the grid fell to the bottom of the well, allowing sample adsorption to the carbon-coated side.

The grid was incubated with the sample for 90 min at 4℃. It was then removed from the drop and washed in a 50 µL drop of cryo-EM-friendly buffer (10 mM HEPES pH 7.5, 1 mM EDTA, 5 mM $MgCl_2$, 150 mM NaCl, 10 mM KCl, 3% trehalose). We gently blotted the grid using filter paper and added 4 µL of cryo-EM-friendly Buffer before mounting the grid onto a Thermo Fisher Scientific Vitrobot Mk. IV set to 100% humidity, cooled to 4℃ and loaded with Whatman Grade 1 Qualitative Filter Paper (GE Healthcare). The grid was immediately blotted for 10 sec (blot force 10) and plunge-frozen in liquid ethane.

Data Collection

The grid was loaded onto a Titan Krios cryo-electron microscope (Thermo Fisher Scientific) operating at 300 kV and equipped with a K3 direct electron detector camera (Gatan) mounted behind a BioQuantum energy filter (Gatan). Electron micrographs were acquired as dose-fractionated movies (11,134 movies in total) in super-resolution counting mode with the microscope set to 80,879x magnification (corresponding to a pixel size of 0.9386 Å) and a total electron exposure of 50 $e^-/Å^2$. Defocus values ranged from -0.9 to -2.5 µm. Automated data collection was controlled by SerialEM. For high-throughput data collection, we used image shift with active beam tilt correction enabled to collect 20 movies at each stage position. All other parameters can be found in Table S1.

Data Processing

All processing steps were performed using RELION 3.1(*43*) unless otherwise indicated. Movies were imported into RELION and classified into 5 optics groups according to the respective beam shift used during acquisition. Alignment of the movie frames was performed using MotionCor2(*45*) and GCTF(*44*) was used for fitting of the contrast transfer function and defocus estimation. To ensure that we captured particles in all poses present on the grid, we used the unbiased Laplacian-of-Gaussian autopicker(*50*) in RELION for particle picking. Instead of 2D classification, an initial 3D classification (with C4 symmetry applied) was performed in order to prevent loss of rare views that might be classified into classes containing broken particles or false-positive particle picks in 2D classification. An initial reconstruction of the ROQ1-XopQ complex generated in cryoSPARC(*51*) from a grid quality screening session was used as the reference model. The particles from the best classes in this initial 3D classification were subjected to successive rounds of alignment-free 3D classification, and alignment-free 2D classification for each 3D class, followed by removal of bad particles and 3D refinement. This enabled us to recover the side views of the ROQ1-XopQ complex, which we failed to do using alternative processing approaches. A final round of 3D-refinement and alignment-free 3D classification (tau = 16) yielded one high-quality class containing 15,263 particles, with a broad distribution of projection directions. After CTF-refinement and Bayesian polishing (*50*) of these particles, 3D-refinement resulted in a reconstruction of the ROQ1-XopQ complex at 3.8 Å resolution overall (FSC = 0.143). This initial map was of sufficient quality for atomic model building of the NB-ARC region (NBD-HD1-WHD) as well as the most N-terminal portion of the LRR. Further processing was needed to improve the LRR-PL-XopQ and TIR domain regions. To resolve the interaction between ROQ1 and XopQ, we applied symmetry expansion to our particles and performed a focused refinement using a mask around one LRR-PL-XopQ module. The angular search space was restricted to preserve the particle orientations after symmetry expansion. The resulting reconstruction converged to 3.8 Å resolution, displaying clear separation between β-strand of the LRR and PL, as well as densities for the sidechains that interact with XopQ.

To improve the TIR domain map, we applied signal subtraction to our particles using a 3D mask around the TIR domains and selected particles exhibiting good density in this region by alignment-free 3D classification. This improved the overall signal for the TIR domain but the features of the density were too poor to confidently fit a model into this four-fold symmetric map. We reasoned that the poor map quality might originate from a symmetry mismatch between the TIR domains and the remainder of the complex, with the TIR domains possibly assuming lower symmetry. Therefore, we applied symmetry expansion to the particles subset and classified the data using alignment-free classification after signal subtraction to remove everything except the TIR domains from the particle images. The particles split equally into two identical classes rotated 90° relative to each other, revealing four TIR domains forming a dimer of dimers with C2 symmetry. Focused refinement of the TIR and NB-ARC regions (the signal from TIR domains alone was too small for proper particle alignment) improved the overall resolution to 4.6 Å, but the NB-ARC region is better resolved than the TIR domains. Based on local resolution estimation, the resolution of the TIR domains is around 7.5 Å, with the highest resolution features observed at the interface between the TIR domains. The onset of phase randomisation leads to an artifact in the corrected half-map FSC curve. For the graphical representation, we have removed three points of the FSC curves near 20 Å resolution to correct for this.

Model Building and Refinement

Each of the three cryo-EM maps (NB-ARC region, LRR-PL-XopQ module, and TIR domains) were used separately to build atomic models of the different parts of the ROQ1-XopQ complex. Initially, a model generated using SWISS-MODEL(*52*) based on the structure of ZAR1 NBD (PDB: 6J5T) was docked into our cryo-EM map using UCSF Chimera (61). This model served as a starting point to build the structure of the NB-ARC domain manually in COOT(*46*). Our initial map of the ROQ1-XopQ complex was used to build residues 189-625 of ROQ1 as well as for fitting the ATP ligand. The map resulting from the focused classification around the LRR-PL-XopQ region was then used to build the following C-terminal residues of ROQ1. We used the secondary-structure prediction algorithm in Phyre2(*53*) to guide us in building our model, specifically matching densities of β-strands and α-helices to sequences of residues with a corresponding predicted secondary structure. In a few cases, poorly resolved linker regions between β-strands were left unmodeled. We used the densities of large side chains and nearby secondary structure elements to ensure correct register assignment of the residues that followed. The structure of the open conformation of XopQ from *Xanthomonas oryzae pv. oryzae* (PDB: 4KL0) was used to fit XopQ into our density. The minor sequence differences with XopQ from *Xanthomonas euvesicatoria* were fixed in COOT(*46*).

A model for the ROQ1 TIR domain was generated in SWISS-MODEL(*52*) using the structure of the plant RPV1 TIR domain (PDB: 5KU7), as it shares the most sequence similarity among published structures. Four individual TIR domain monomers were docked in the TIR domain map using Chimera(*54*) and modified in COOT(*46*) to properly fit the density.

The atomic models for the TIR domain, the NB-ARC domain and LRR-PL-XopQ region were each refined in their respective maps with successive rounds of real-space refinement in PHENIX(*47*). Iterative rounds of rigid-body refinement, morphing and gradient driven global minimization were used in the initial stages of refinement while applying ramachandran, rotamer, C_β, and secondary structure restraints throughout to maintain good model geometry at the resolution of our cryo-EM maps. Internal symmetry was imposed on the NB-ARC model and the TIR domain model. Structural issues were corrected manually in COOT(*46*) between rounds of refinement. The final model was refined using atomic displacement parameter refinement and gradient driven global minimization while applying the same restraint as described previously. The model was validated using MOLPROBITY(*55*) within PHENIX(*47*), and the model vs. map FSC was calculated using the MTRIAGE(*48*) validation tool in PHENIX(*47*).

HR Phenotype and Protein Expression

The various ROQ1 mutants were made and constructed into PE1776 vectors fusing with a C-terminal 3Flag tag. For HR phenotype observation, ROQ1 mutants and StrepII-XopQ were transiently co-expressed in *N. tabacum roq1-1* mutant leaves via agrobacterium mediated transformation. HR phenotypes were observed and imaged 2 days post infiltration. To detect protein expressions, ROQ1 mutants and StrepII-XopQ were co-expressed in *N. benthamiana eds1-1* mutant leaves, extracted using protein extraction buffer (50 mM Tris-HCl, pH 7.5, 150 mM NaCl, 1mM EDTA, 0.2% Nonidet P-40, 0.2%Triton X-100, 6 mM β-mercaptoethanol, 10mM DTT and 1×Protease Inhibitor Cocktail), boiled in Laemmli buffer for 5 min and separated on 8% SDS-PAGE gels. StrepII-XopQ were detected with the primary StrepTag II monoclonal antibody (A02230, Abbkine) and the second antibody (A4416, Sigma). ROQ1 mutants were enriched by ANTI-FLAG M2 Affinity Gel (A2220, Sigma-Aldrich) before boiled, and detected with the primary monoclonal anti-Flag antibody (F1804, Sigma-Aldrich) and the second antibody (A4416, Sigma).

Conservation of the Roq1 C-JID

The conservation scores for each residue in the C-JID of Roq1 (1129-1306) were calculated in Consurf (52). Unique homologous sequences with a sequence identity between 20% and 95% were collected from UNIREF90 using 3 iterations of the PSI-BLAST search algorithm (E-value: 0.0001). The 38 unique sequences found were aligned using MAFFT(*56*). In some regions, too few sequences aligned to calculate a reliable conservation score (positions occupied by fewer than 6 amino acids in the multiple sequence alignment are deemed to have unreliable scores) and were colored in gray. This occurred in our alignment at positions 1179-1200 (corresponding to a part of the NR loop of Roq1 that recognizes XopQ’s active site) for which only 2 homologues found were aligned with. An alignment file is provided in the supplementary material (Sequence alignment file S1).

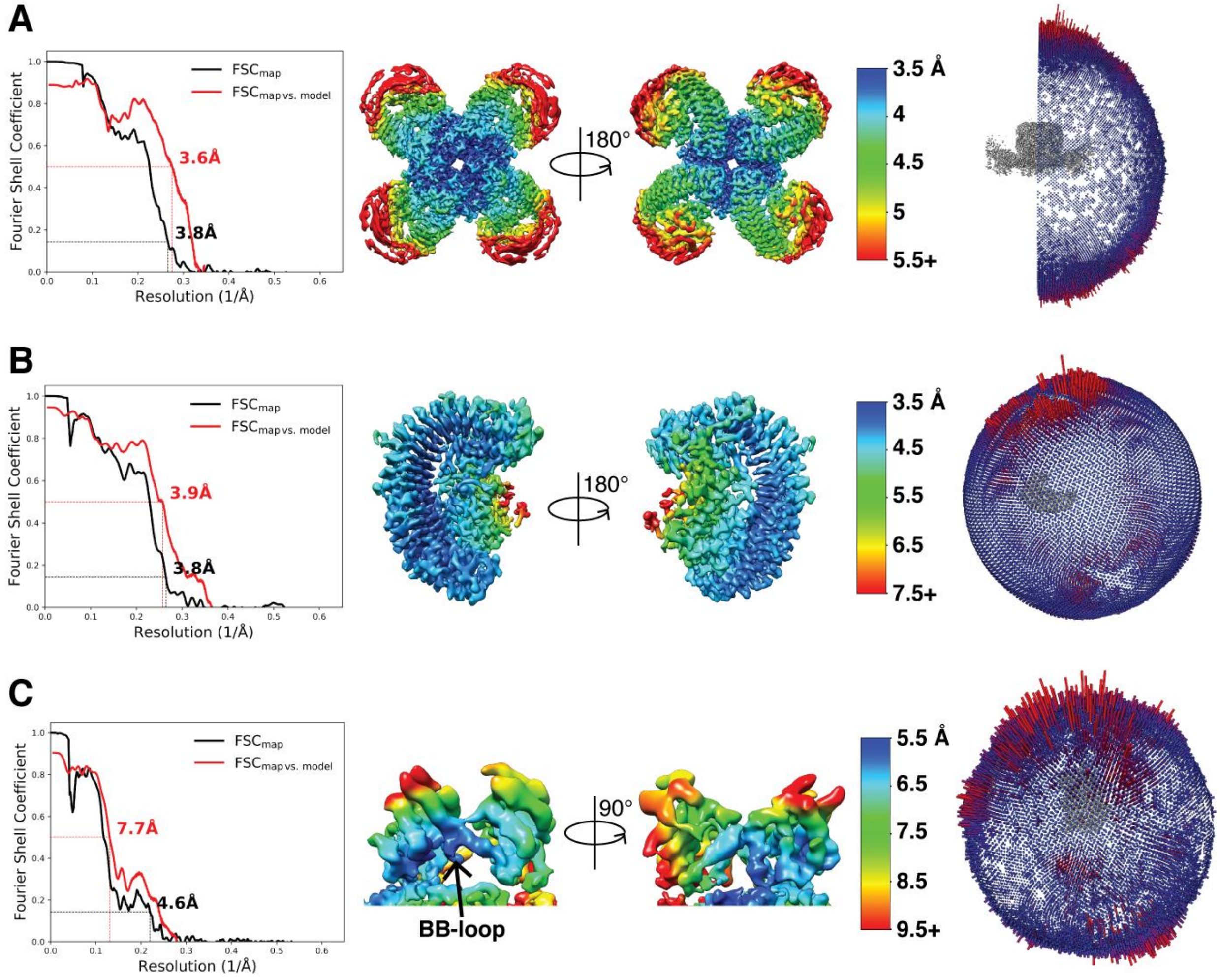

Fig. S1.

Resolution estimation. Left: map FSC and map vs model FSC for the three reconstructions used to build the atomic model of the ROQ1-XopQ complex. Right: Local resolution for each map. (A) Map vs model FSC calculated using residues 189-625 of ROQ1, corresponding to the NB-ARC and the N-terminal region of the LRR. (B) Map vs model FSC calculated using residues 526-1303 of ROQ1, corresponding to the LRR-PL region, and 89-453 of XopQ. (C) Map vs model FSC calculated using residues 11-176 of ROQ1, corresponding to the TIR domain.

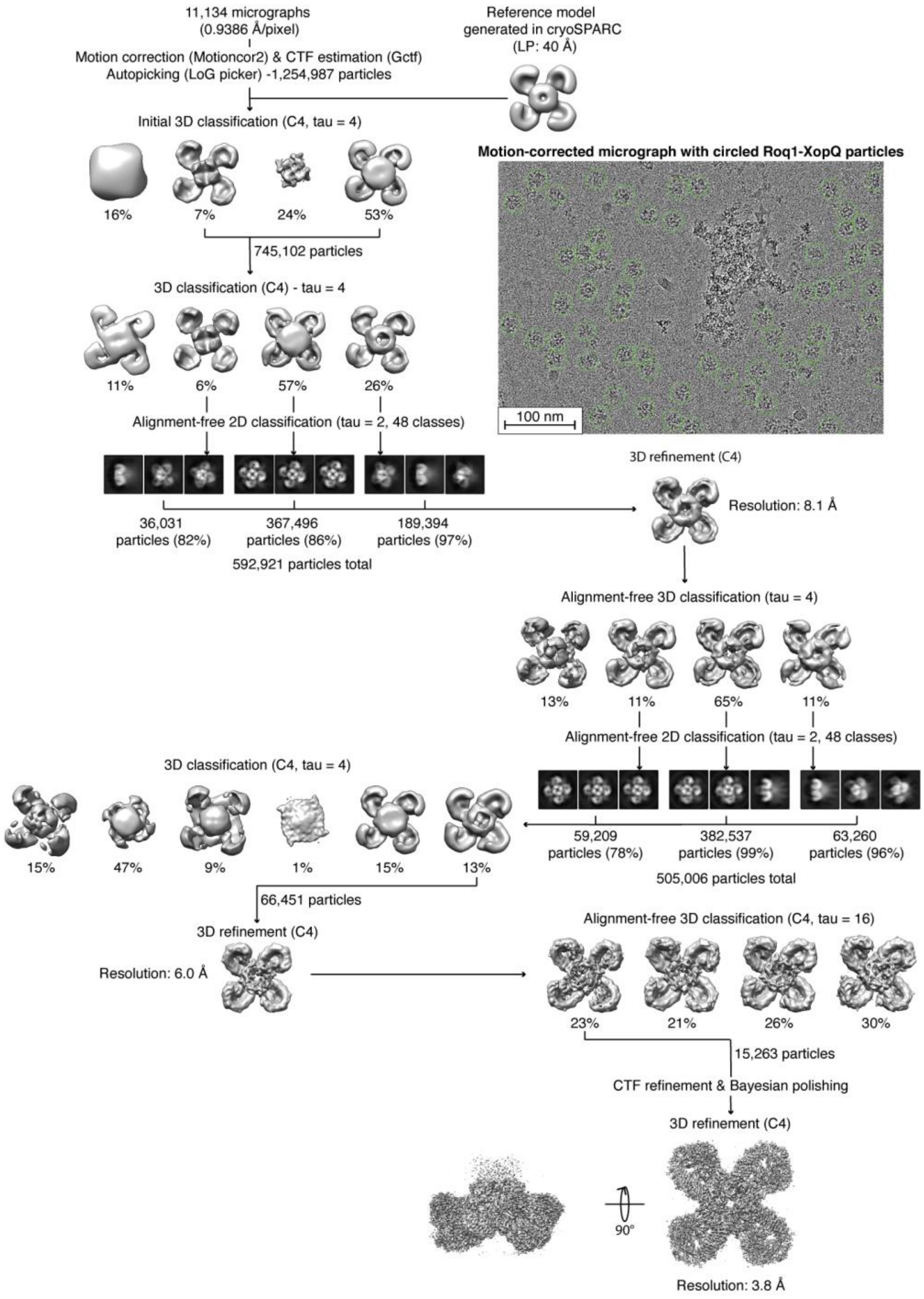

Fig. S2.

Cryo-EM data processing tree from collected EM movies to the initial reconstruction of the ROQ1-XopQ complex.

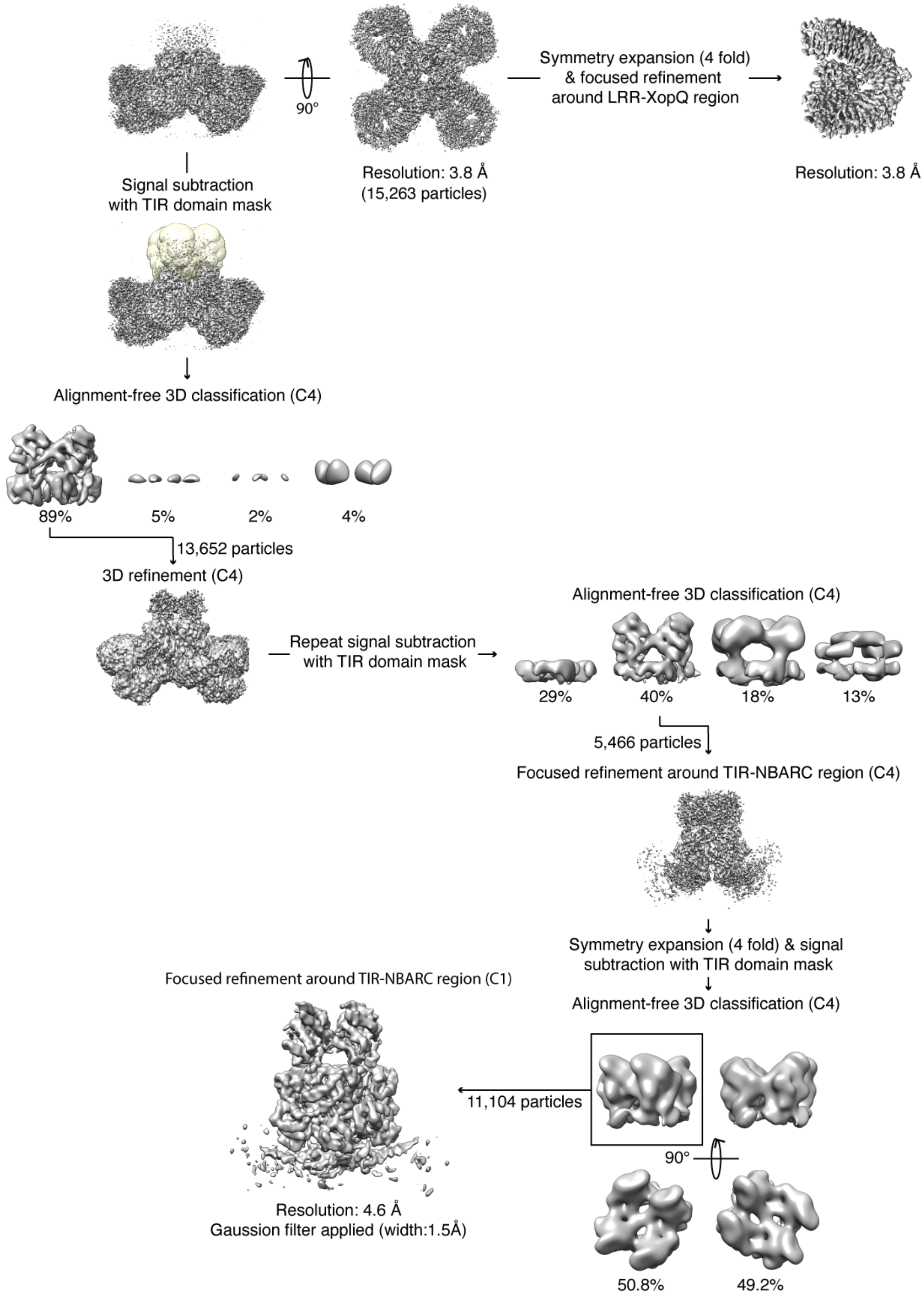

Fig. S3.

Further cryo-EM data processing needed to resolve the LRR-PL-XopQ region and the TIR domains.

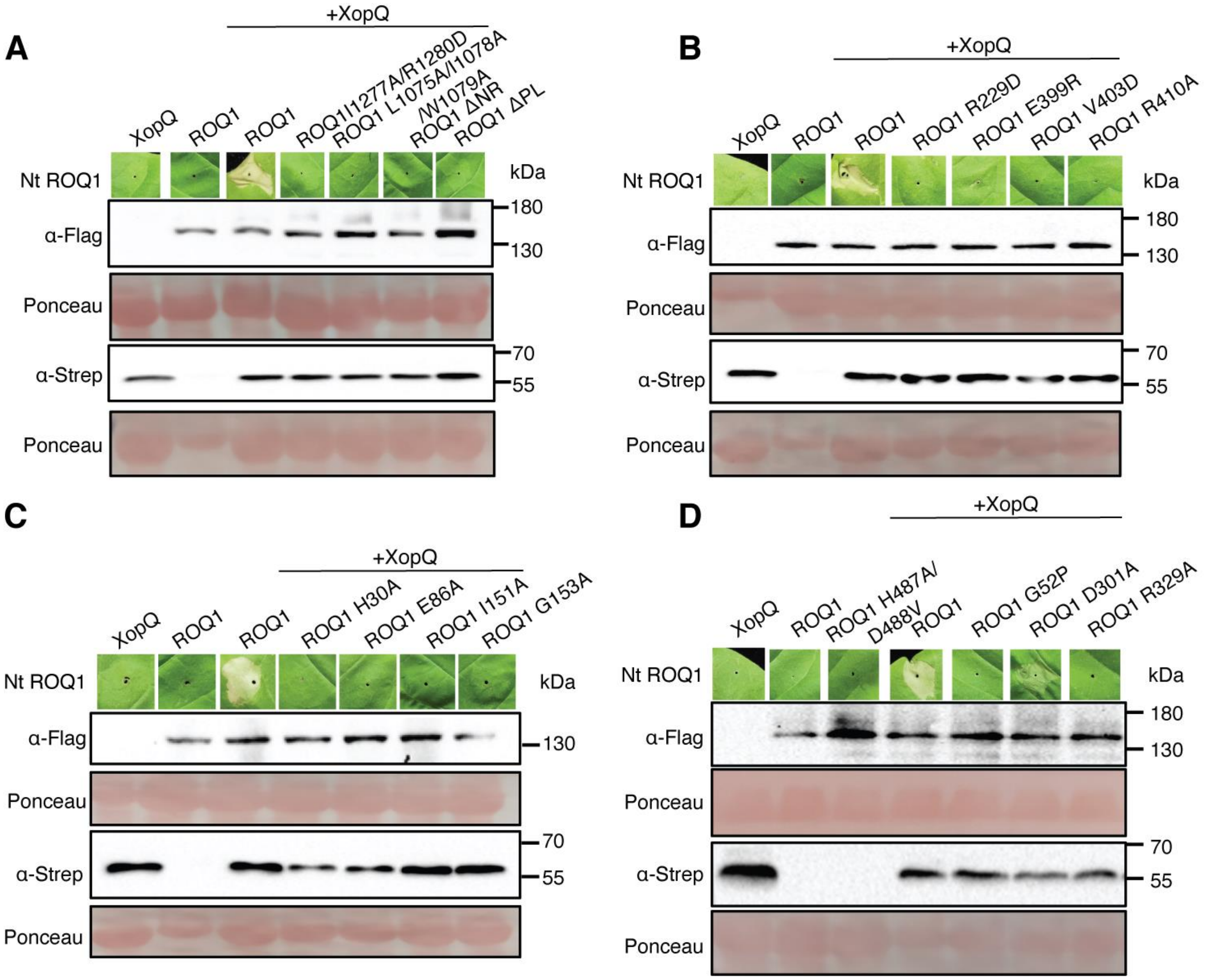

Fig. S4.

HR Phenotype and Protein Expression of ROQ1 mutants. The HR phenotype is detected on the leaf tissue at the site of agrobacterium injection (top row). Expression of ROQ1 and XopQ was detected by Western-blotting using an anti-Flag antibody and an anti-StrepTagII antibody respectively. Ponceau staining was used for the detection of protein bands on the Western-blots. (A) Mutation in the LRR-PL-XopQ interface. Residues providing contacts between XopQ and the LRR (ROQ1 L1075A/I1078A/W1079A) as well between XopQ and the PL domain (ROQ1 I1277A/ R1280D, ΔNR and ΔPL) were mutated. For the ΔNR mutant, residues corresponding to the NR loop of Roq1 (1163-1195) were replaced with a flexible linker with the following sequence: SGGGSGGS. For the ΔPL mutant, the C-terminal end of ROQ1 (1129-1306), corresponding to the PL domain, was truncated. (B) Mutations at the oligomerization interface of ROQ1 in the NB-ARC domain. More specifically, the R229 is at the NDB-NBD interface and E399, V403 and R410 are at the HD1-WHD interface. (C) Mutations in the TIR domain of ROQ1 at the AE (H30A) and BE (I151A, G153A) interfaces. The catalytic glutamate in the active site of the TIR domain (E86) was mutated to an alanine. (D) Additional mutations: in the MHD motif (H487A/D488V), the TIR domain BB-loop glycine (G52P), the Walker B motif (D301A) and the TTR motif (R329A).

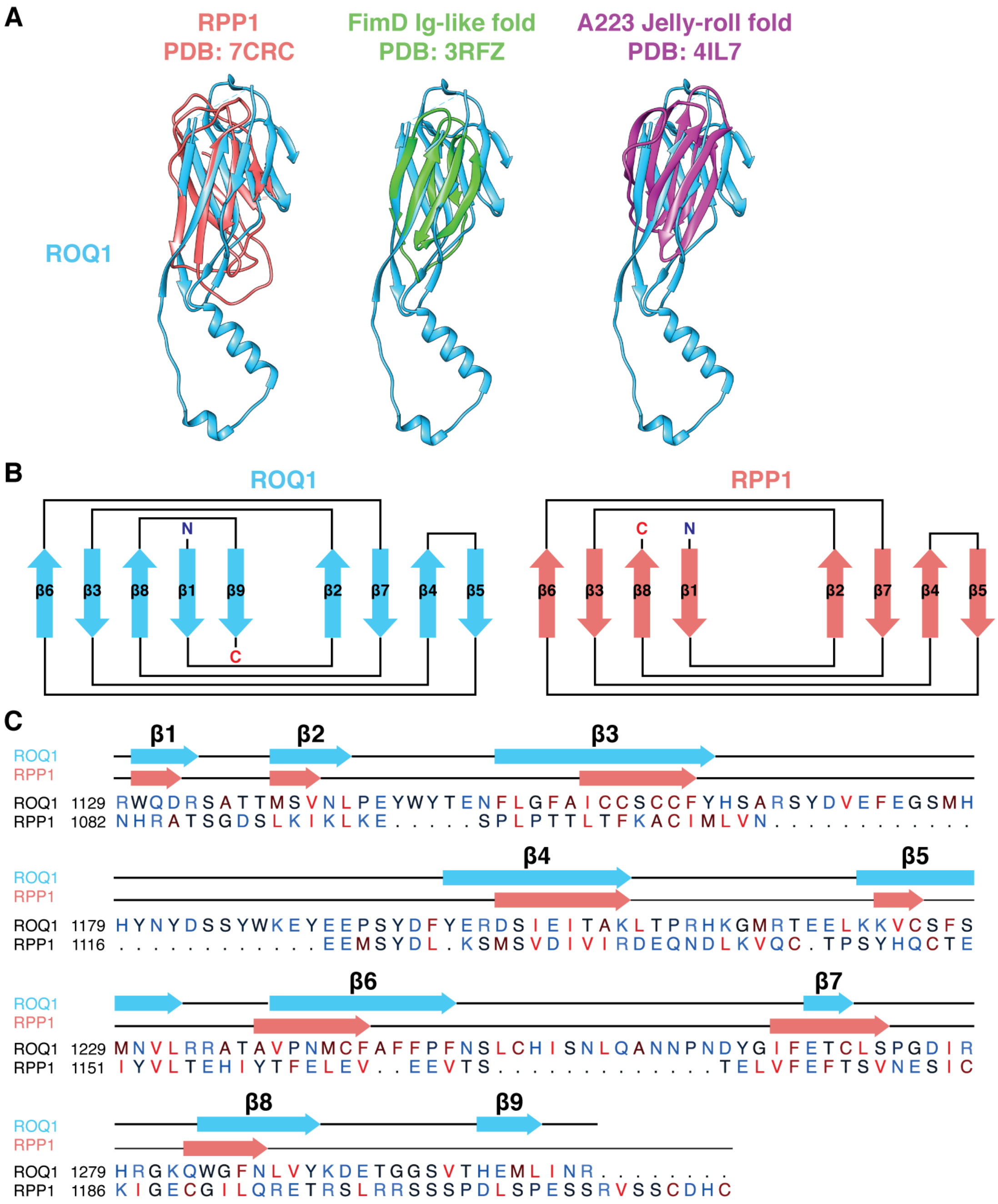

Fig. S5.

Comparison between the ROQ1 C-JID (PL domain) and the RPP1 C-JID. (A) From left to right: Structural alignment of the ROQ1 C-JID with the RPP1 C-JID (PDB: 7CRC), the Ig-like fold in FimD (PDB: 3RFZ), and the Jelly-roll fold in A223 (PDB: 4IL7). FimD and A223 were among the highest scoring structural homologous of the ROQ1 C-JID found using the CATH database (*17*) and were used as representatives of their respective folds. (B) β-stand topology of ROQ1 (left) and RPP1 (right). The only difference found is at the 9th β-stand of ROQ1 which does not appear in the RPP1 structure. (C) Local sequence alignment between the ROQ1 C-JID (1129-1306) and the RPP1 C-JID (1082-1221). Positions of the β-stands in ROQ1 and RPP1 are labeled along the sequence using the same color code as in panel B. Residues are colored according to the Kyte-Doolittle hydrophobicity scale (*57*), with polar residues colored in blue, intermediate residues in black and hydrophobic residues colored in red. Alignment was performed using the Smith-Waterman algorithm (*58*).

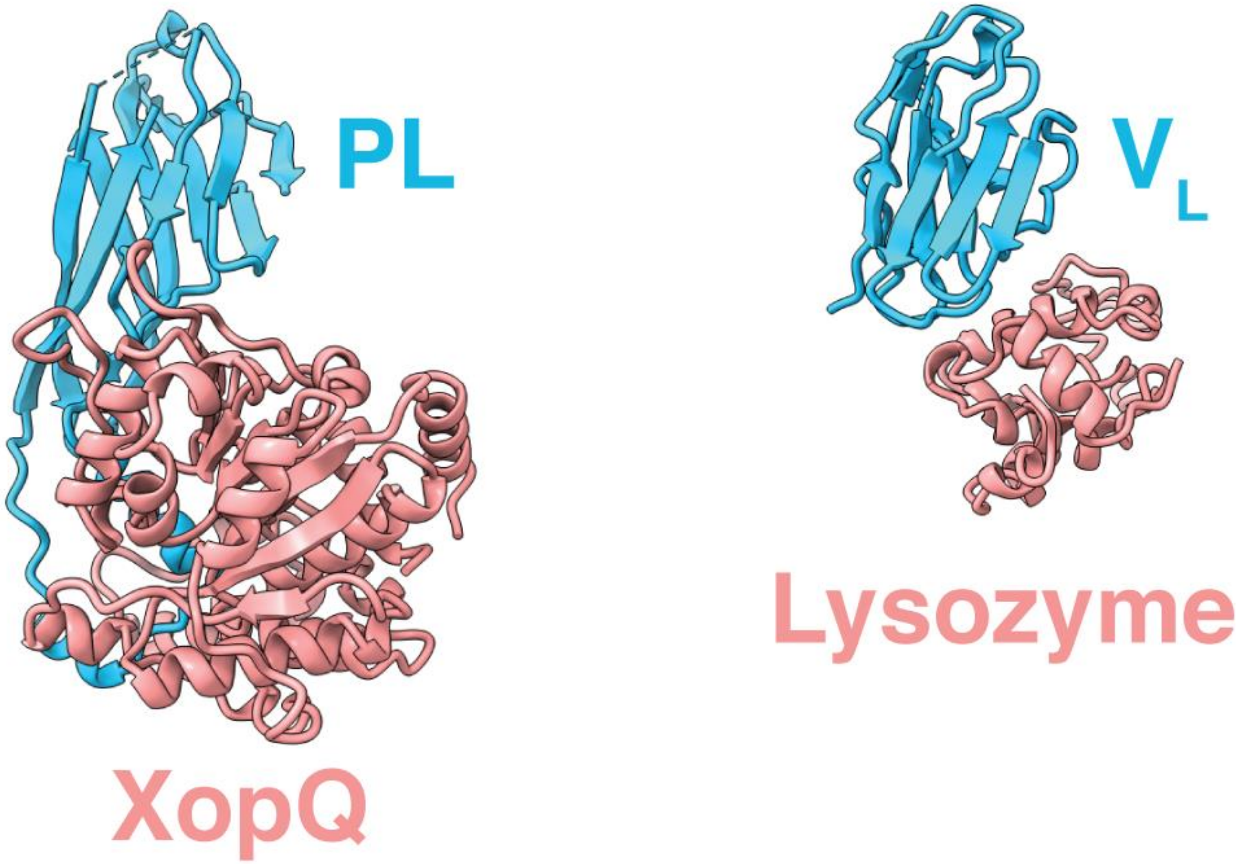

Fig. S6.

Comparison between the C-JID domain of ROQ1 recognizing XopQ (left) and the light-chain variable fragment (V_L) of an antibody recognizing lysozyme (PDB: 3HFM) (right). Loops emerging from the β-sandwich of either the C-JID or V_L (light blue) interact with the substrate (salmon).

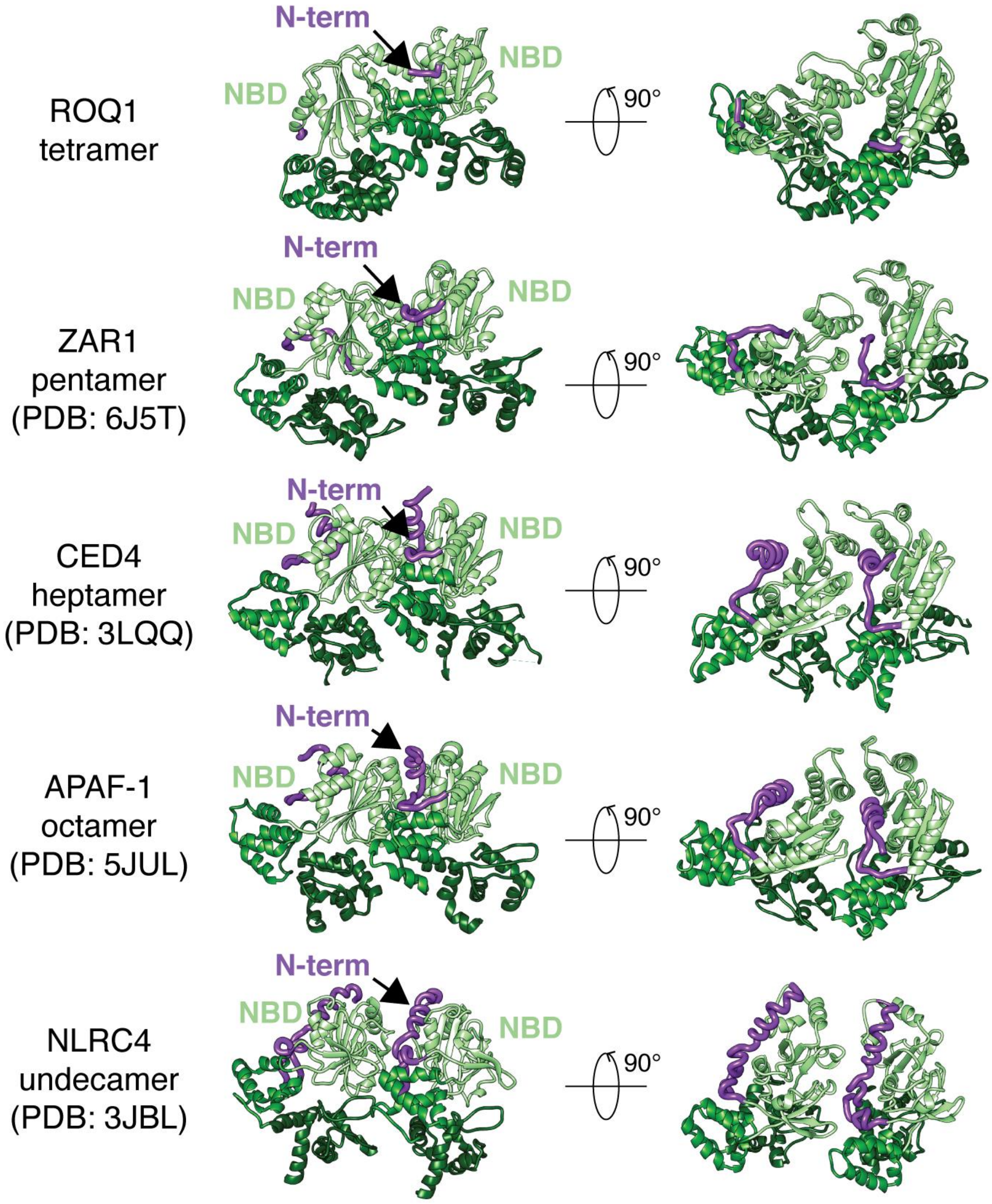

Fig. S7.

Structure of the NBD N-terminal linker (purple) in activated NLRs with increasing oligomeric states. The NBD-HD1-WHD of two neighboring protomers is shown (following the color scheme of ROQ1), with the N-terminal linker of the NBD wedged between them.

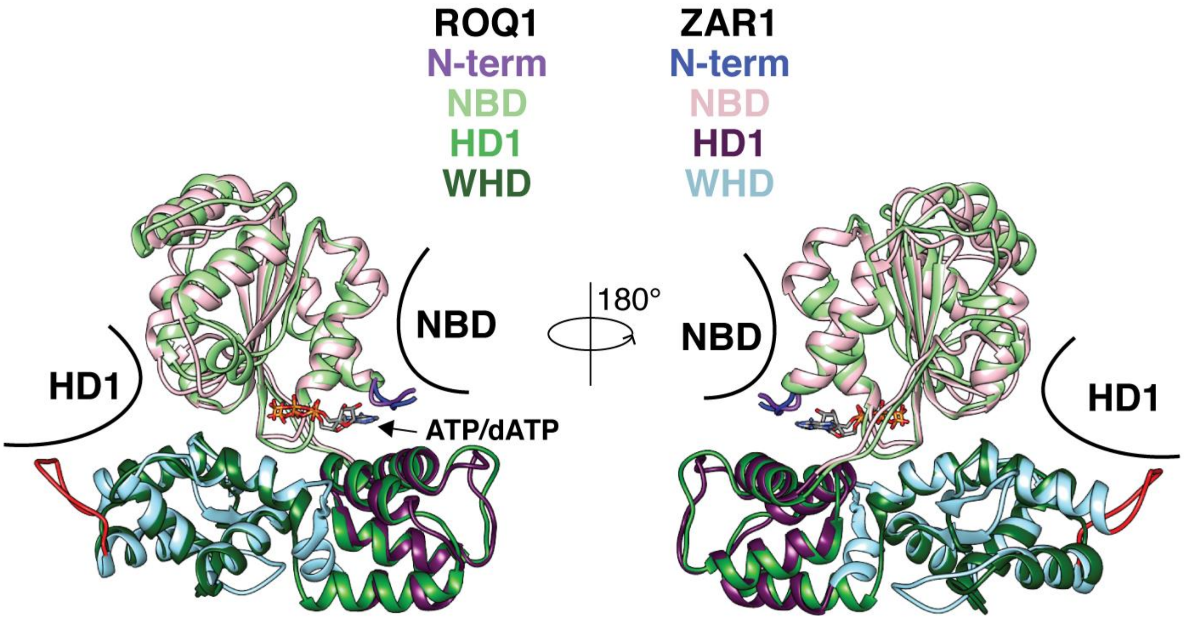

Fig. S8.

Structural comparison between the NB-ARC domain of ROQ1 and ZAR1 in the oligomerized state. The NBD and HD1 of neighboring subunits are represented in black. The NBD and HD1 closely align to each other, whereas we find differences in the loops of the WHD, with one of them extending to make contacts with the neighboring HD1 (red). This loop compensates for the increased distance between the WHD and HD1 in the ZAR1 pentamer relative to the ROQ1 tetramer.

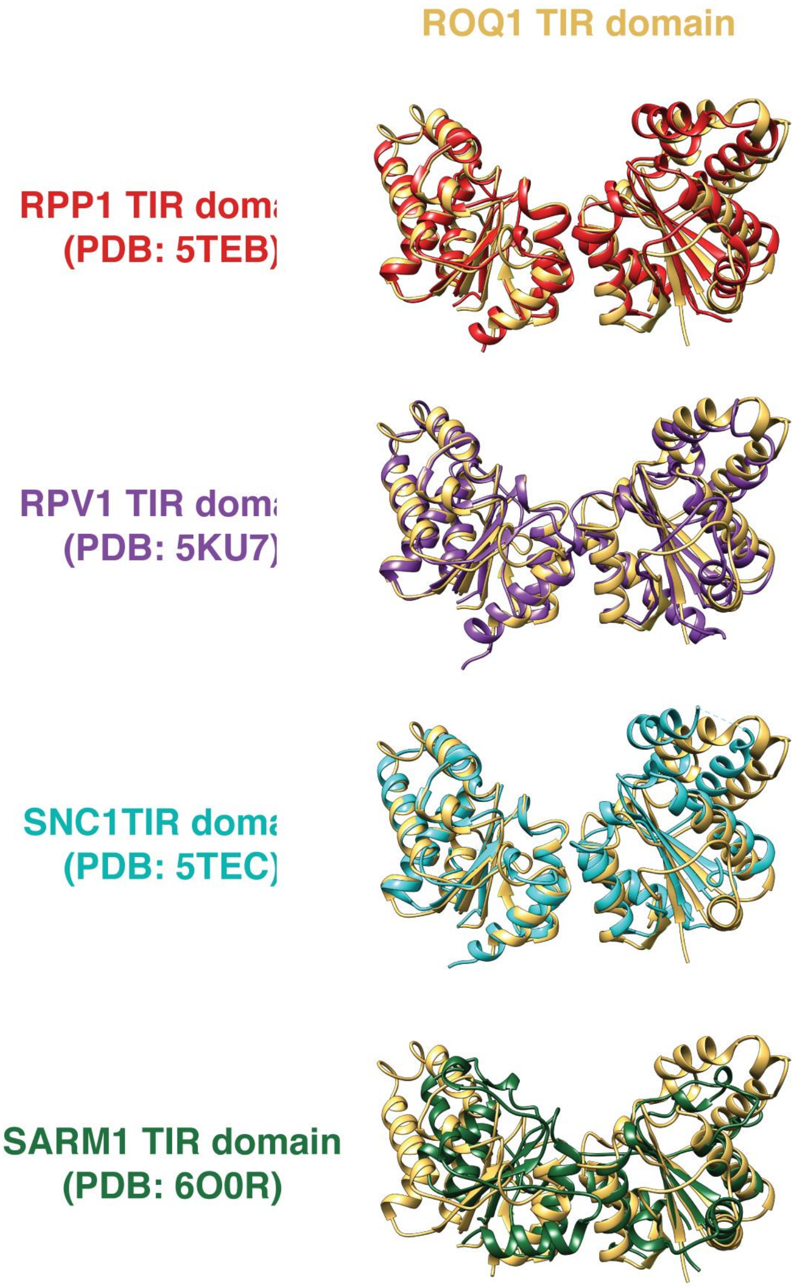

Fig. S9.

Structural comparison between the ROQ1 TIR AE interface and the AE interface found in the crystal lattice of other TIR domains.

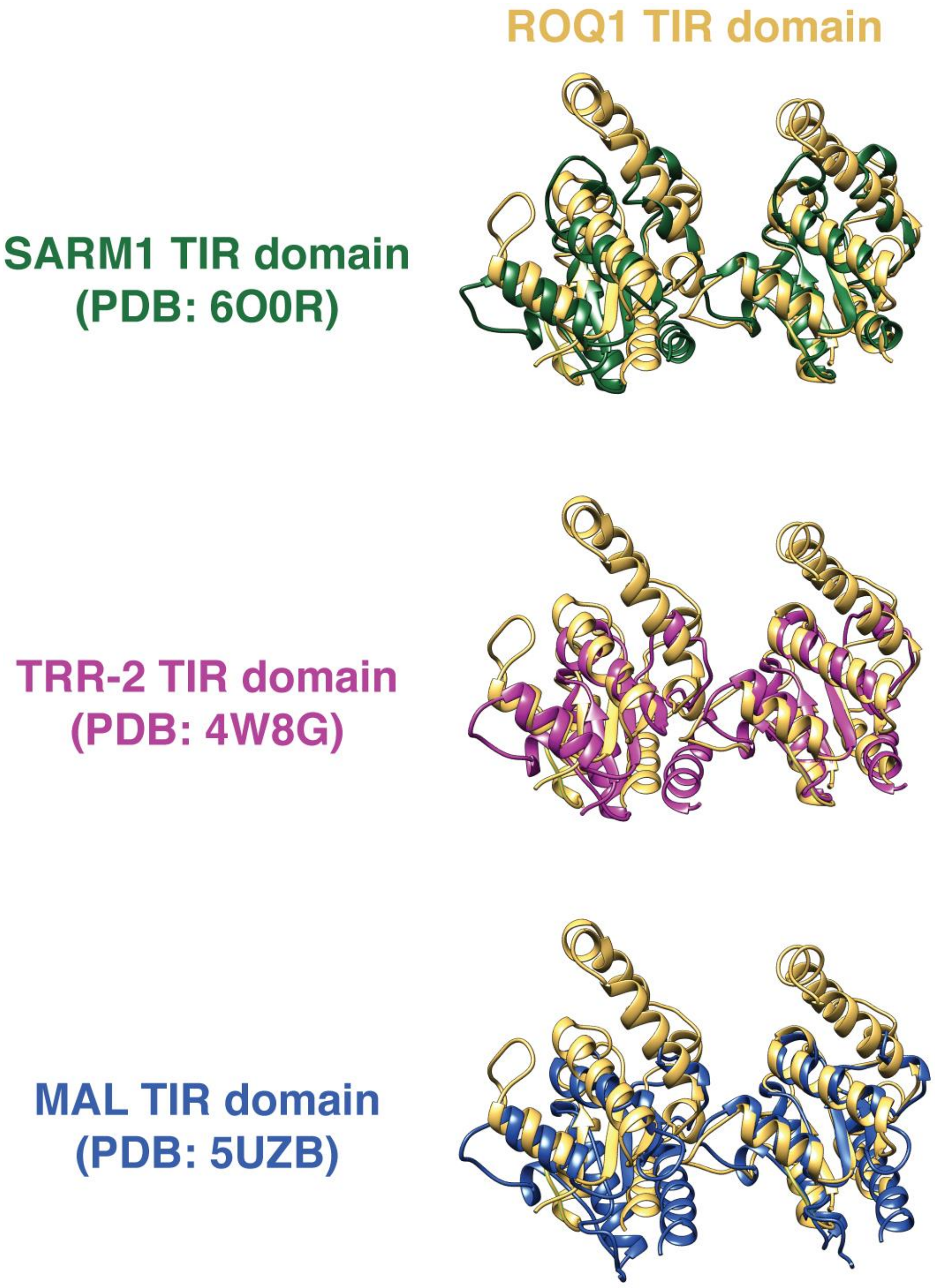

Fig. S10.

Structural comparison between the ROQ1 TIR BE interface and the BE interface found in the crystal lattice of metazoan TIR domains.

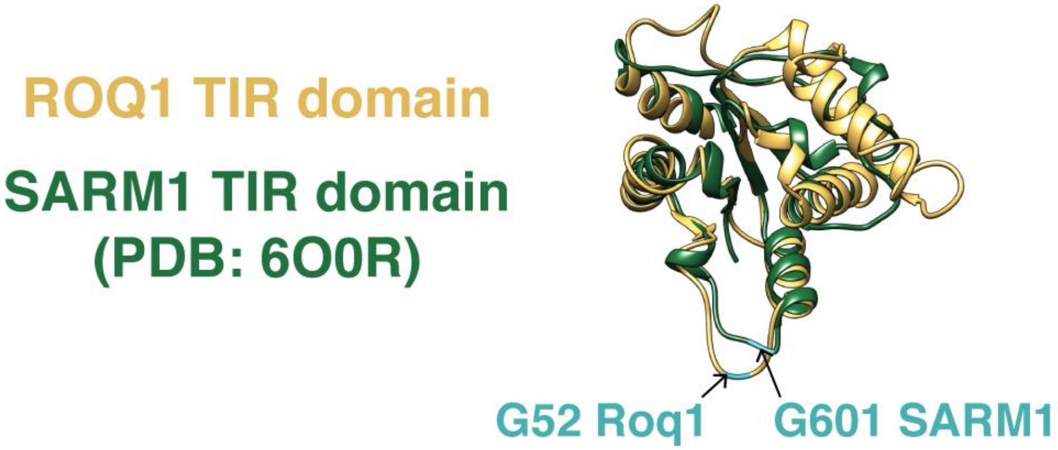

Fig. S11.

Position of the BB-loop glycine in both ROQ1 and SARM1 TIR domains. Glycines are represented in cyan.

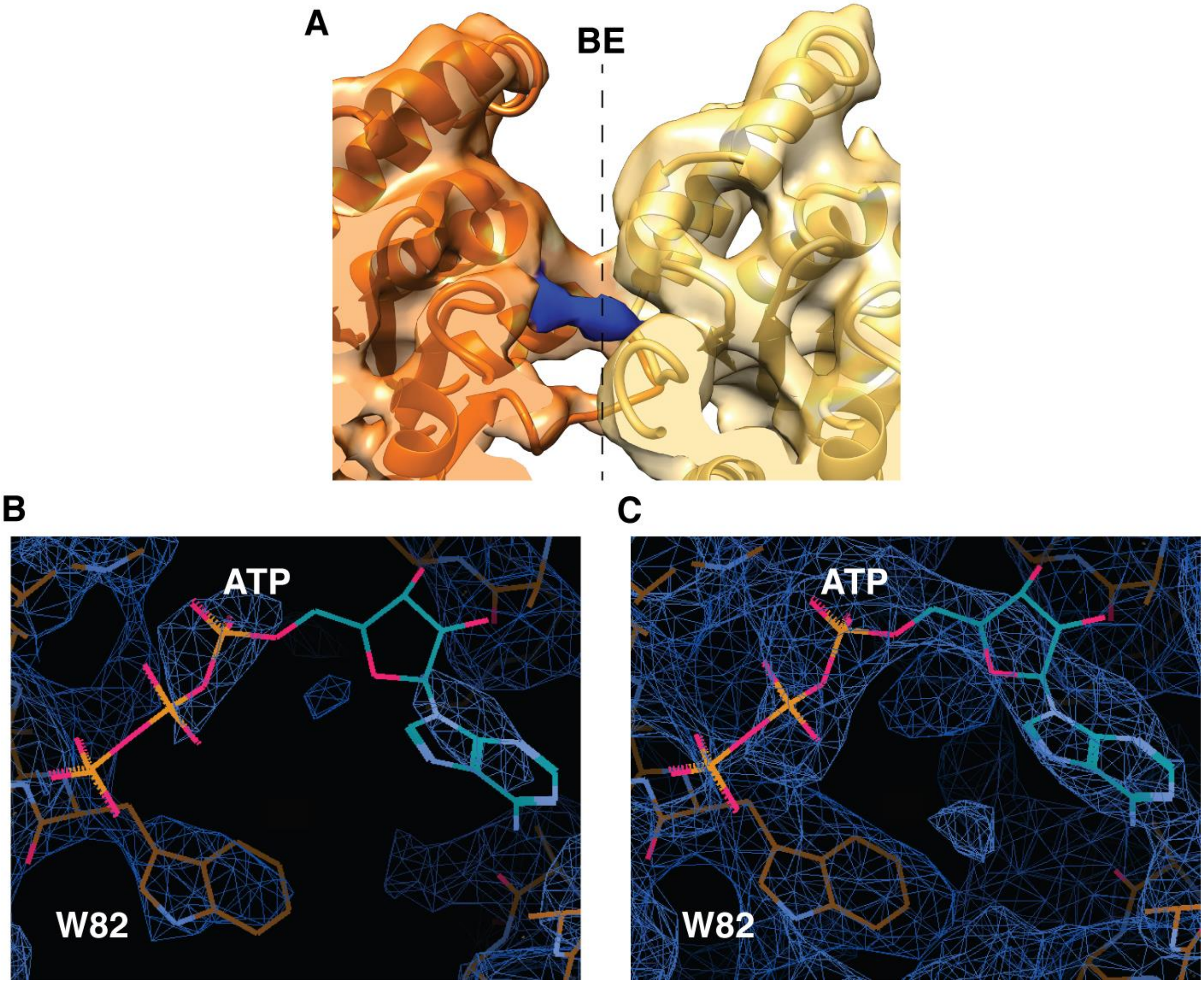

Fig. S12.

A small unidentified density is observed above the TIR domain active site. (A) Two TIR domains at the BE-interface with the unidentified density (blue) in between them. The BB-loop of the TIR domain on the left (orange) is in the engaged state, leaving the NADase active site open. A gaussian filter was applied to the map (width 1.5 Å) to reduce noise. (B,C) An ATP molecule was placed within the unidentified density shown at different contour levels. The nearby tryptophan (W82) density can be used to compare signal strength. While density for W82 is clearly visible at low threshold, density for a hypothetical ATP is very weak. At a higher threshold, for which there is density that could account for the base, ribose, α-phosphate and part of the β-phosphate of ATP, the density corresponding to W82 is overblown and noise is visible.

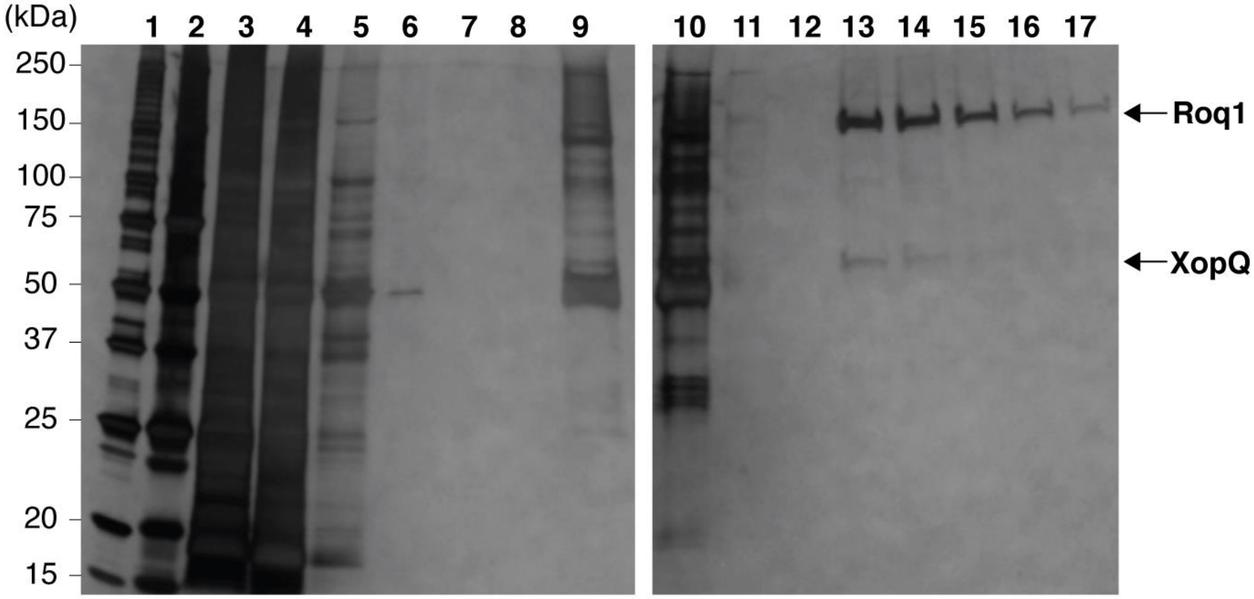

1: 0.5 µL Ladder (Bio-Rad Precision Plus Protein Unstained Standards)
2: 2.5 µL Ladder
3: Lysed cells
4: Flowthrough after binding Roq1-Flag to ANTI-FLAG M2 affinity gel (Sigma-Aldrich)
5-8: Successive washes of ANTI-FLAG M2 affinity gel
9: Elution from ANTI-FLAG M2 affinity gel
10: Flowthrough after binding StrepII-XopQ to Strep-Tactin Superflow Plus resin (Qiagen)
11-12: Successive washes of Strep-Tactin Superflow Plus resin
13-17: Successive elutions from Strep-Tactin Superflow Plus resin (10 µL loaded)

Fig. S13.

Purification of the ROQ1-XopQ complex. Samples were analyzed by SDS-PAGE and silver stained.

Data Collection

Microscope	Krios
Voltage (kV)	300
Detector	K3
Magnification	80,879x
Energy filter slit (eV)	25
Movies	11,134
Pixel size (Å)	0.9386
Defocus range (µm)	-0.9 to -2.5
Exposure (e$^-$/Å^2)	50
Exposure rate (e$^-$/Å^2/frame)	1
Automation software	SerialEM

Reconstruction

Region	Initial reconstruction	LRR-PL-XopQ	TIR domains
Software	RELION	RELION	RELION
Particles (initial)	1,254,987	1,254,987	1,254,987
Particles (final)	15,263	15,263	5,466
Box size (pixels)	480	480	480
Accuracy rotations (°)	0.84	1.28	1.94
Accuracy translations (Å)	0.63	0.98	1.2
Map resolution (Å) FSC = 0.143/0.5	3.8/4.4	3.8/4.4	4.6/8.3
Map sharpening B-factor (Å^2)	-82	-67	-97
Local resolution range (Å)	3.4-9.3	3.8-9.7	5.3-24.6

Coordinate Refinement

Software	PHENIX	PHENIX	PHENIX
Resolution Cutoff	3.6	3.8	6
FSC model vs. map = 0.5 (Å)	3.6	3.9	7.7
Model vs. map CC (global/local)	0.80/0.82	0.78/0.78	0.44/0.43

Model

Number of residues

Protein	1748	1079	664
Ligands	8 (4 ATP & 4 Mg^{2+})	1 (Ca^{2+})	None

B-factor (Å^2)

Protein	39	65	194
Ligand	31	47	N/A

R.m.s deviations

Bonds lenghts (Å)	0.003	0.003	0.001
Bond angles (°)	0.74	0.772	0.417

Validation

Molprobity score	1.97	2.11	1.52
Molprobity clashscore	9.27	11.55	2.96
Rotamer outliers (%)	0	0.21	0
C$_\beta$ deviations (%)	0	0	0

Ramachandran plot

Favored (%)	92.18	90.72	93.29
Allowed (%)	7.82	9.28	6.71
Outliers (%)	0	0	0
CaBLAM outliers (%)	7.16	5.69	2.47
EM ringer score	1.74	1.46	N/A (C$_\alpha$ only)

Deposition

PDB	7JLV	7JLU	7JLX
EMDB	22381	22380	22383

Table S1.

Cryo-EM data collection, data processing, model refinement and validation statistics.

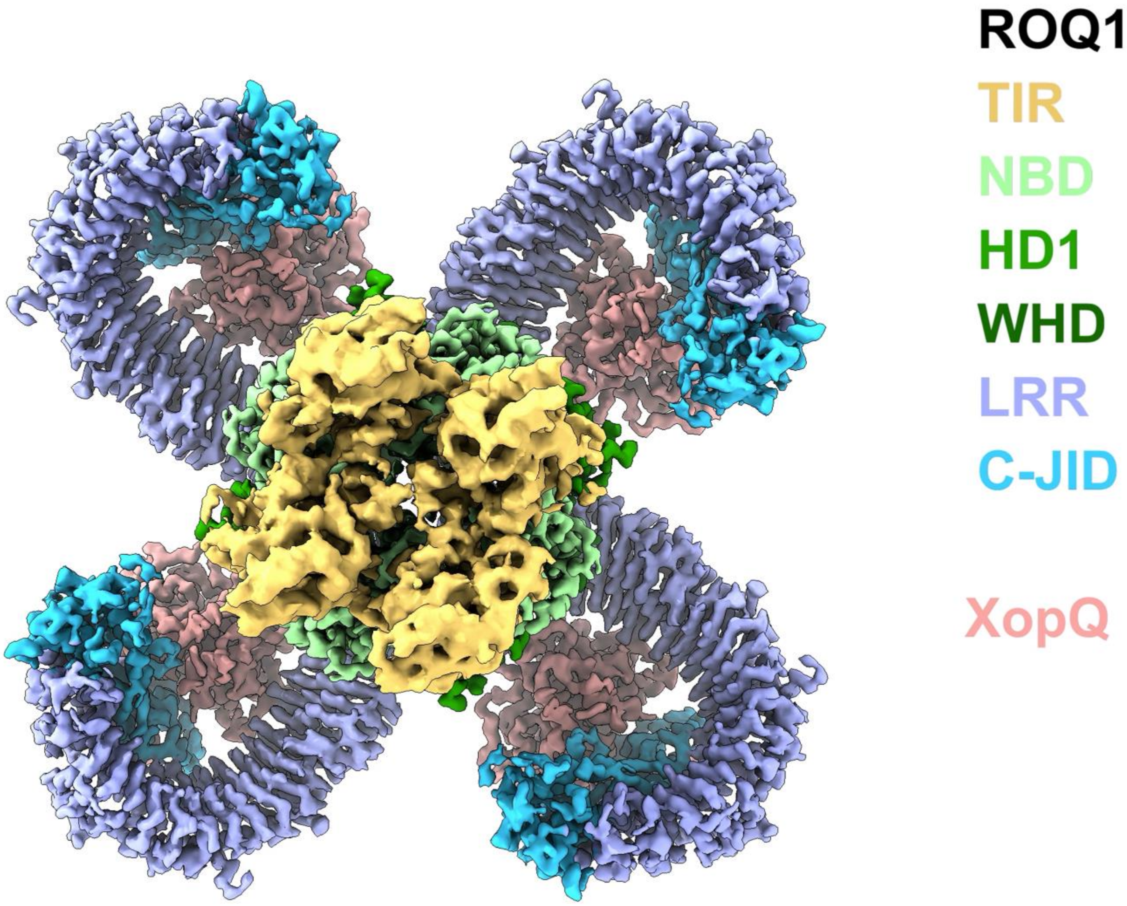

Movie S1.

Cryo-EM density map and atomic model of the ROQ1-XopQ complex with colors corresponding to the different protein domains (as in Fig. 1). Regions of interest are zoomed in to highlight the different features of the structure.

References and Notes

1. J. L. Dangl, D. M. Horvath, B. J. Staskawicz, Pivoting the plant immune system from dissection to deployment. *Science* **341**, 746–751 (2013). doi:10.1126/science.1236011 Medline

2. J. Wang, J. Chai, Structural insights into the plant immune receptors PRRs and NLRs. *Plant Physiol.* **182**, 1566–1581 (2020). doi:10.1104/pp.19.01252 Medline

3. J. Tamborski, K. V. Krasileva, Evolution of plant NLRs: From natural history to precise modifications. *Annu. Rev. Plant Biol.* **71**, 355–378 (2020). doi:10.1146/annurev-arplant-081519-035901 Medline

4. J. M. Feehan, B. Castel, A. R. Bentham, J. D. G. Jones, Plant NLRs get by with a little help from their friends. *Curr. Opin. Plant Biol.* **56**, 99–108 (2020). doi:10.1016/j.pbi.2020.04.006 Medline

5. L. M. Jubic, S. Saile, O. J. Furzer, F. El Kasmi, J. L. Dangl, Help wanted: Helper NLRs and plant immune responses. *Curr. Opin. Plant Biol.* **50**, 82–94 (2019). doi:10.1016/j.pbi.2019.03.013 Medline

6. J. D. G. Jones, R. E. Vance, J. L. Dangl, Intracellular innate immune surveillance devices in plants and animals. *Science* **354**, aaf6395 (2016). doi:10.1126/science.aaf6395 Medline

7. J. Wang, J. Wang, M. Hu, S. Wu, J. Qi, G. Wang, Z. Han, Y. Qi, N. Gao, H.-W. Wang, J.-M. Zhou, J. Chai, Ligand-triggered allosteric ADP release primes a plant NLR complex. *Science* **364**, eaav5868 (2019). doi:10.1126/science.aav5868 Medline

8. J. Wang, M. Hu, J. Wang, J. Qi, Z. Han, G. Wang, Y. Qi, H. W. Wang, J. M. Zhou, J. Chai, Reconstitution and structure of a plant NLR resistosome conferring immunity. *Science* **364**, eaav5870 (2019). doi:10.1126/science.aav5870 Medline

9. L. Wan, K. Essuman, R. G. Anderson, Y. Sasaki, F. Monteiro, E.-H. Chung, E. Osborne Nishimura, A. DiAntonio, J. Milbrandt, J. L. Dangl, M. T. Nishimura, TIR domains of plant immune receptors are NAD^+-cleaving enzymes that promote cell death. *Science* **365**, 799–803 (2019). doi:10.1126/science.aax1771 Medline

10. S. Horsefield, H. Burdett, X. Zhang, M. K. Manik, Y. Shi, J. Chen, T. Qi, J. Gilley, J.-S. Lai, M. X. Rank, L. W. Casey, W. Gu, D. J. Ericsson, G. Foley, R. O. Hughes, T. Bosanac, M. von Itzstein, J. P. Rathjen, J. D. Nanson, M. Boden, I. B. Dry, S. J. Williams, B. J. Staskawicz, M. P. Coleman, T. Ve, P. N. Dodds, B. Kobe, NAD^+ cleavage activity by animal and plant TIR domains in cell death pathways. *Science* **365**, 793–799 (2019). doi:10.1126/science.aax1911 Medline

11. A. Schultink, T. Qi, A. Lee, A. D. Steinbrenner, B. Staskawicz, Roq1 mediates recognition of the Xanthomonas and Pseudomonas effector proteins XopQ and HopQ1. *Plant J.* **92**, 787–795 (2017). doi:10.1111/tpj.13715 Medline

12. T. Qi, K. Seong, D. P. T. Thomazella, J. R. Kim, J. Pham, E. Seo, M.-J. Cho, A. Schultink, B. J. Staskawicz, NRG1 functions downstream of EDS1 to regulate TIR-NLR-mediated plant immunity in *Nicotiana benthamiana*. *Proc. Natl. Acad. Sci. U.S.A.* **115**, E10979–E10987 (2018). doi:10.1073/pnas.1814856115 Medline

13. D. Lapin, D. D. Bhandari, J. E. Parker, Origins and immunity networking functions of EDS1 family proteins. *Annu. Rev. Phytopathol.* **58**, 253–276 (2020). doi:10.1146/annurev-phyto-010820-012840 Medline

14. S. Yu, I. Hwang, S. Rhee, The crystal structure of type III effector protein XopQ from Xanthomonas oryzae complexed with adenosine diphosphate ribose. *Proteins* **82**, 2910–2914 (2014). doi:10.1002/prot.24656 Medline

15. L. Liu, I. Botos, Y. Wang, J. N. Leonard, J. Shiloach, D. M. Segal, D. R. Davies, Structural basis of toll-like receptor 3 signaling with double-stranded RNA. *Science* **320**, 379–381 (2008). doi:10.1126/science.1155406 Medline

16. C. Van Ghelder, D. Esmenjaud, TNL genes in peach: Insights into the post-LRR domain. *BMC Genomics* **17**, 317 (2016). doi:10.1186/s12864-016-2635-0 Medline

17. I. Sillitoe, N. Dawson, T. E. Lewis, S. Das, J. G. Lees, P. Ashford, A. Tolulope, H. M. Scholes, I. Senatorov, A. Bujan, F. Ceballos Rodriguez-Conde, B. Dowling, J. Thornton, C. A. Orengo, CATH: Expanding the horizons of structure-based functional annotations for genome sequences. *Nucleic Acids Res.* **47** (D1), D280–D284 (2019). doi:10.1093/nar/gky1097 Medline

18. S. Ma, D. Lapin, L. Liu, Y. Sun, W. Song, X. Zhang, E. Logemann, D. Yu, J. Wang, J. Jirschitzka, Z. Han, P. Schulze-Lefert, J. E. Parker, J. Chai, Direct pathogen-induced assembly of an NLR immune receptor complex to form a holoenzyme. *Science* 10.1126/science.abe3069 (2020). doi:10.1126/science.abe3069

19. W. Li, Y.-H. Chiang, G. Coaker, The HopQ1 effector's nucleoside hydrolase-like domain is required for bacterial virulence in arabidopsis and tomato, but not host recognition in tobacco. *PLOS ONE* **8**, e59684 (2013). doi:10.1371/journal.pone.0059684 Medline

20. N. Adlung, U. Bonas, Dissecting virulence function from recognition: Cell death suppression in Nicotiana benthamiana by XopQ/HopQ1-family effectors relies on EDS1-dependent immunity. *Plant J.* **91**, 430–442 (2017). doi:10.1111/tpj.13578 Medline

21. Y. Xiong, Z. Han, J. Chai, Resistosome and inflammasome: Platforms mediating innate immunity. *Curr. Opin. Plant Biol.* **56**, 47–55 (2020). doi:10.1016/j.pbi.2020.03.010 Medline

22. J. F. C. Steele, R. K. Hughes, M. J. Banfield, Structural and biochemical studies of an NB-ARC domain from a plant NLR immune receptor. *PLOS ONE* **14**, e0221226 (2019). doi:10.1371/journal.pone.0221226 Medline

23. Z. Hu, C. Yan, P. Liu, Z. Huang, R. Ma, C. Zhang, R. Wang, Y. Zhang, F. Martinon, D. Miao, H. Deng, J. Wang, J. Chang, J. Chai, Crystal structure of NLRC4 reveals its autoinhibition mechanism. *Science* **341**, 172–175 (2013). doi:10.1126/science.1236381 Medline

24. Y. Pang, X. C. Bai, C. Yan, Q. Hao, Z. Chen, J. W. Wang, S. H. W. Scheres, Y. Shi, Structure of the apoptosome: Mechanistic insights into activation of an initiator caspase from Drosophila. *Genes Dev.* **29**, 277–287 (2015). doi:10.1101/gad.255877.114 Medline

25. S. Qi, Y. Pang, Q. Hu, Q. Liu, H. Li, Y. Zhou, T. He, Q. Liang, Y. Liu, X. Yuan, G. Luo, H. Li, J. Wang, N. Yan, Y. Shi, Crystal structure of the *Caenorhabditis elegans* apoptosome

reveals an octameric assembly of CED-4. *Cell* **141**, 446–457 (2010). doi:10.1016/j.cell.2010.03.017 Medline

26. J. L. Tenthorey, N. Haloupek, J. R. López-Blanco, P. Grob, E. Adamson, E. Hartenian, N. A. Lind, N. M. Bourgeois, P. Chacón, E. Nogales, R. E. Vance, The structural basis of flagellin detection by NAIP5: A strategy to limit pathogen immune evasion. *Science* **358**, 888–893 (2017). doi:10.1126/science.aao1140 Medline

27. L. Zhang, S. Chen, J. Ruan, J. Wu, A. B. Tong, Q. Yin, Y. Li, L. David, A. Lu, W. L. Wang, C. Marks, Q. Ouyang, X. Zhang, Y. Mao, H. Wu, Cryo-EM structure of the activated NAIP2-NLRC4 inflammasome reveals nucleated polymerization. *Science* **350**, 404–409 (2015). doi:10.1126/science.aac5789 Medline

28. V. Bonardi, K. Cherkis, M. T. Nishimura, J. L. Dangl, A new eye on NLR proteins: Focused on clarity or diffused by complexity? *Curr. Opin. Immunol.* **24**, 41–50 (2012). doi:10.1016/j.coi.2011.12.006 Medline

29. X. Yang, F. Yang, W. Wang, G. Lin, Z. Hu, Z. Han, Y. Qi, L. Zhang, J. Wang, S.-F. Sui, J. Chai, Structural basis for specific flagellin recognition by the NLR protein NAIP5. *Cell Res.* **28**, 35–47 (2018). doi:10.1038/cr.2017.148 Medline

30. E. F. Halff, C. A. Diebolder, M. Versteeg, A. Schouten, T. H. C. Brondijk, E. G. Huizinga, Formation and structure of a NAIP5-NLRC4 inflammasome induced by direct interactions with conserved N- and C-terminal regions of flagellin. *J. Biol. Chem.* **287**, 38460–38472 (2012). doi:10.1074/jbc.M112.393512 Medline

31. A. M. Bayless, M. T. Nishimura, Enzymatic functions for Toll/interleukin-1 receptor domain proteins in the plant immune system. *Front. Genet.* **11**, 539 (2020). doi:10.3389/fgene.2020.00539 Medline

32. X. Zhang, M. Bernoux, A. R. Bentham, T. E. Newman, T. Ve, L. W. Casey, T. M. Raaymakers, J. Hu, T. I. Croll, K. J. Schreiber, B. J. Staskawicz, P. A. Anderson, K. H. Sohn, S. J. Williams, P. N. Dodds, B. Kobe, Multiple functional self-association interfaces in plant TIR domains. *Proc. Natl. Acad. Sci. U.S.A.* **114**, E2046–E2052 (2017). doi:10.1073/pnas.1621248114 Medline

33. S. J. Williams, K. H. Sohn, L. Wan, M. Bernoux, P. F. Sarris, C. Segonzac, T. Ve, Y. Ma, S. B. Saucet, D. J. Ericsson, L. W. Casey, T. Lonhienne, D. J. Winzor, X. Zhang, A. Coerdt, J. E. Parker, P. N. Dodds, B. Kobe, J. D. G. Jones, Structural basis for assembly and function of a heterodimeric plant immune receptor. *Science* **344**, 299–303 (2014). doi:10.1126/science.1247357 Medline

34. K.-G. Hyun, Y. Lee, J. Yoon, H. Yi, J.-J. Song, Crystal structure of Arabidopsis thaliana SNC1 TIR domain. *Biochem. Biophys. Res. Commun.* **481**, 146–152 (2016). doi:10.1016/j.bbrc.2016.11.004 Medline

35. M. Bernoux, T. Ve, S. Williams, C. Warren, D. Hatters, E. Valkov, X. Zhang, J. G. Ellis, B. Kobe, P. N. Dodds, Structural and functional analysis of a plant resistance protein TIR domain reveals interfaces for self-association, signaling, and autoregulation. *Cell Host Microbe* **9**, 200–211 (2011). doi:10.1016/j.chom.2011.02.009 Medline

36. S. J. Williams, L. Yin, G. Foley, L. W. Casey, M. A. Outram, D. J. Ericsson, J. Lu, M. Boden, I. B. Dry, B. Kobe, Structure and function of the TIR domain from the grape NLR

protein RPV1. *Front. Plant Sci.* **7**, 1850 (2016). Medline

37. Y. Xu, X. Tao, B. Shen, T. Horng, R. Medzhitov, J. L. Manley, L. Tong, Structural basis for signal transduction by the Toll/interleukin-1 receptor domains. *Nature* **408**, 111–115 (2000). doi:10.1038/35040600 Medline

38. S. Nimma, T. Ve, S. J. Williams, B. Kobe, Towards the structure of the TIR-domain signalosome. *Curr. Opin. Struct. Biol.* **43**, 122–130 (2017). doi:10.1016/j.sbi.2016.12.014 Medline

39. L. Vyncke, C. Bovijn, E. Pauwels, T. Van Acker, E. Ruyssinck, E. Burg, J. Tavernier, F. Peelman, Reconstructing the TIR side of the myddosome: A paradigm for TIR-TIR interactions. *Structure* **24**, 437–447 (2016). doi:10.1016/j.str.2015.12.018 Medline

40. T. Ve, P. R. Vajjhala, A. Hedger, T. Croll, F. DiMaio, S. Horsefield, X. Yu, P. Lavrencic, Z. Hassan, G. P. Morgan, A. Mansell, M. Mobli, A. O'Carroll, B. Chauvin, Y. Gambin, E. Sierecki, M. J. Landsberg, K. J. Stacey, E. H. Egelman, B. Kobe, Structural basis of TIR-domain-assembly formation in MAL- and MyD88-dependent TLR4 signaling. *Nat. Struct. Mol. Biol.* **24**, 743–751 (2017). doi:10.1038/nsmb.3444 Medline

41. K. Essuman, D. W. Summers, Y. Sasaki, X. Mao, A. K. Y. Yim, A. DiAntonio, J. Milbrandt, TIR domain proteins are an ancient family of NAD$^+$-consuming enzymes. *Curr. Biol.* **28**, 421–430.e4 (2018). doi:10.1016/j.cub.2017.12.024 Medline

42. Y. Wu, J. Kuzma, E. Maréchal, R. Graeff, H. C. Lee, R. Foster, N. H. Chua, Abscisic acid signaling through cyclic ADP-ribose in plants. *Science* **278**, 2126–2130 (1997). doi:10.1126/science.278.5346.2126 Medline

43. S. H. W. Scheres, RELION: Implementation of a Bayesian approach to cryo-EM structure determination. *J. Struct. Biol.* **180**, 519–530 (2012). doi:10.1016/j.jsb.2012.09.006 Medline

44. K. Zhang, Gctf: Real-time CTF determination and correction. *J. Struct. Biol.* **193**, 1–12 (2016). doi:10.1016/j.jsb.2015.11.003 Medline

45. S. Q. Zheng, E. Palovcak, J.-P. Armache, K. A. Verba, Y. Cheng, D. A. Agard, MotionCor2: Anisotropic correction of beam-induced motion for improved cryo-electron microscopy. *Nat. Methods* **14**, 331–332 (2017). doi:10.1038/nmeth.4193 Medline

46. P. Emsley, K. Cowtan, Coot: Model-building tools for molecular graphics. *Acta Crystallogr. D Biol. Crystallogr.* **60**, 2126–2132 (2004). doi:10.1107/S0907444904019158 Medline

47. P. D. Adams, R. W. Grosse-Kunstleve, L. W. Hung, T. R. Ioerger, A. J. McCoy, N. W. Moriarty, R. J. Read, J. C. Sacchettini, N. K. Sauter, T. C. Terwilliger, PHENIX: Building new software for automated crystallographic structure determination. *Acta Crystallogr. D Biol. Crystallogr.* **58**, 1948–1954 (2002). doi:10.1107/S0907444902016657 Medline

48. P. V. Afonine, B. P. Klaholz, N. W. Moriarty, B. K. Poon, O. V. Sobolev, T. C. Terwilliger, P. D. Adams, A. Urzhumtsev, New tools for the analysis and validation of cryo-EM maps and atomic models. *Acta Crystallogr. D Struct. Biol.* **74**, 814–840 (2018). doi:10.1107/S2059798318009324 Medline

49. H. Ashkenazy, S. Abadi, E. Martz, O. Chay, I. Mayrose, T. Pupko, N. Ben-Tal, ConSurf

2016: An improved methodology to estimate and visualize evolutionary conservation in macromolecules. *Nucleic Acids Res.* **44** (W1), W344–W350 (2016). doi:10.1093/nar/gkw408 Medline

50. J. Zivanov, T. Nakane, B. O. Forsberg, D. Kimanius, W. J. Hagen, E. Lindahl, S. H. Scheres, New tools for automated high-resolution cryo-EM structure determination in RELION-3. *eLife* **7**, e42166 (2018). doi:10.7554/eLife.42166 Medline
51. A. Punjani, J. L. Rubinstein, D. J. Fleet, M. A. Brubaker, cryoSPARC: Algorithms for rapid unsupervised cryo-EM structure determination. *Nat. Methods* **14**, 290–296 (2017). doi:10.1038/nmeth.4169 Medline
52. A. Waterhouse, M. Bertoni, S. Bienert, G. Studer, G. Tauriello, R. Gumienny, F. T. Heer, T. A. P. de Beer, C. Rempfer, L. Bordoli, R. Lepore, T. Schwede, SWISS-MODEL: Homology modelling of protein structures and complexes. *Nucleic Acids Res.* **46** (W1), W296–W303 (2018). doi:10.1093/nar/gky427 Medline
53. L. A. Kelley, S. Mezulis, C. M. Yates, M. N. Wass, M. J. E. Sternberg, The Phyre2 web portal for protein modeling, prediction and analysis. *Nat. Protoc.* **10**, 845–858 (2015). doi:10.1038/nprot.2015.053 Medline
54. E. F. Pettersen, T. D. Goddard, C. C. Huang, G. S. Couch, D. M. Greenblatt, E. C. Meng, T. E. Ferrin, UCSF Chimera—A visualization system for exploratory research and analysis. *J. Comput. Chem.* **25**, 1605–1612 (2004). doi:10.1002/jcc.20084 Medline
55. C. J. Williams, J. J. Headd, N. W. Moriarty, M. G. Prisant, L. L. Videau, L. N. Deis, V. Verma, D. A. Keedy, B. J. Hintze, V. B. Chen, S. Jain, S. M. Lewis, W. B. Arendall 3rd, J. Snoeyink, P. D. Adams, S. C. Lovell, J. S. Richardson, D. C. Richardson, MolProbity: More and better reference data for improved all-atom structure validation. *Protein Sci.* **27**, 293–315 (2018). doi:10.1002/pro.3330 Medline
56. K. Katoh, D. M. Standley, MAFFT multiple sequence alignment software version 7: Improvements in performance and usability. *Mol. Biol. Evol.* **30**, 772–780 (2013). doi:10.1093/molbev/mst010 Medline
57. J. Kyte, R. F. Doolittle, A simple method for displaying the hydropathic character of a protein. *J. Mol. Biol.* **157**, 105–132 (1982). doi:10.1016/0022-2836(82)90515-0 Medline
58. T. F. Smith, M. S. Waterman, Identification of common molecular subsequences. *J. Mol. Biol.* **147**, 195–197 (1981). doi:10.1016/0022-2836(81)90087-5 Medline